Title
Body Pressure Image Analyses: Static, Dynamic, and Sensing Strategies for a Pressure Sensitive Bedsheet

Author
Liu, Jason Jun Hing

Publication Date
2014

Peer reviewed|Thesis/dissertation

University of California
Los Angeles

Body Pressure Image Analyses:

Static, Dynamic, and Sensing Strategies for a Pressure Sensitive Bedsheet

A dissertation submitted in partial satisfaction
of the requirements for the degree
Doctor of Philosophy in Computer Science

by

Jason Jun Hing Liu

2014

Abstract of the Dissertation

Body Pressure Image Analyses:
Static, Dynamic, and Sensing Strategies for a Pressure Sensitive Bedsheet

by

Jason Jun Hing Liu

Doctor of Philosophy in Computer Science

University of California, Los Angeles, 2014

Professor Majid Sarrafzadeh, Chair

Ubiquitous personal monitoring of health has rapidly developed in recent years. Technology is playing a major role in the improvement of quality of life. Much of the total expense on healthcare is attributed to chronic illnesses and a large portion can be eliminated through continuous personal monitoring solutions. While pervasive technologies are available now, they need to be as unobtrusive as possible and require as little human intervention as possible. Broad ranges of electronic devices will monitor the human condition and create alert notifications to the individual or care providers.

One new modality in this world of technological advances that can provide major benefit, is a pressure sensitive bedsheet. The resulting pressure images can be analyzed to ascertain information about the person lying on the bed. Questions can be asked, such as what posture is the person sleeping in, or what movement is there? Can we identify and track bodyparts? Can respiration and vital signs be measured? What medical conditions can be detected?

This work investigates some of these questions and contains various methods of analyses through static images and dynamic sequences of motion. Furthermore, methods of sampling strategies are presented with the aim of optimizing the data flow. This work introduces this current research to achieve the aim of continuous personal monitoring using pressure sensitive material.

The dissertation of Jason Jun Hing Liu is approved.

Alex Anh-Tuan Bui

Demetri Terzopoulos

Mario Gerla

Majid Sarrafzadeh, Committee Chair

University of California, Los Angeles

2014

To friends and family

Table of Contents

List of Figures

List of Tables

Acknowledgments

Firstly, I would like to sincerely thank my advisor, Professor Majid Sarrafzadeh, for all his support and guidance. Not only have I learned the right way of doing research but I have also learned that passion and dedication are qualities that will bring out your best.

In addition, I consider Wenyao Xu as my mentor, who is now an Assistant Professor at State University of New York at Buffalo. His advice, knowledge and ideas, along with his friendliness and sense of humor, enabled me to write this thesis. I could not have graduated without him.

I would like to thank my colleagues for their help on various projects. I wish to thank Ming-Chun Huang (now Assistant Professor at Case Western Reserve University), Nabil Alshurafa, Bobak Mortazavi (now Post Doctoral Researcher at Yale), and Lauren Samy, for sharing ideas and assistance along the way. It is an honor to work with them.

My gratitude goes to Medisens Wireless for building and providing the hardware, and also for their feedback and discussions.

I am also very grateful to Professors Mario Gerla, Demetri Terzopoulos, and Alex Bui for being on my thesis committee and providing useful suggestions, which have helped a lot in the development of this work.

Finally, I wish to express my gratitude towards my family. I thank my parents, Doreen and Peter Liu, for their never-ending, unconditional giving and loving. I thank Kara Lee for letting me travel on this road. I thank my boys, Matthew and Daniel, for being my boys.

Vita

1994	B.Sc (Computer Science), University of Sydney
1996	B.E (Electrical Engineering), University of Sydney
2010	M.S.E (Robotics), University of Pennsylvania

Publications

Jason J. Liu, Ming-Chun Huang, Wenyao Xu, Xiaoyi Zhang, Luke Stevens, Nabil Alshurafa and Majid Sarrafzadeh, "**BreathSens: A Continuous On-Bed Respiratory Monitoring System with Torso Localization using an Unobtrusive Pressure Sensing Array**", IEEE Journal of Biomedical and Health Informatics (J-BHI) 2014.

Jason J. Liu, Ming-Chun Huang, Wenyao Xu and Majid Sarrafzadeh, "**Bodypart Localization for Pressure Ulcer Prevention**", IEEE Conference of the Engineering in Medicine and Biology Society (EMBC'14), Chicago, Il, August 2014.

Jason J. Liu, Wenyao Xu, Ming-Chun Huang, Nabil Alshurafa and Majid Sarrafzadeh, Nitin Raut, Behrooz Yadegar, "**Sleep Posture Analysis using a Dense Pressure Sensitive Bedsheet**", Pervasive and Mobile Computing (PMC), Feb 2014.

Ming-Chun Huang, **Jason J. Liu**, Wenyao Xu, Nabil Alshurafa and Majid Sarrafzadeh, "**Using Pressure Map Sequences for Recognition of On Bed Rehabilitation Exercises**", IEEE Journal of Biomedical and Health Informatics (J-BHI) Special Issue, Jan 2014.

Lauren Samy, Ming-Chun Huang, **Jason J. Liu**, Wenyao Xu and Majid Sarrafzadeh, "**Unobtrusive Sleep Stage Identification Using a Pressure Sensitive Bed Sheet**", IEEE Sensors Journal, Jan 2014.

Jason J. Liu, Ming-Chun Huang, Wenyao Xu, Nabil Alshurafa, Majid Sarrafzadeh, "**On-bed Monitoring for Range of Motion Exercises with a Pressure Sensitive Bedsheet**", IEEE International Conference on Implantable and Wearable Body Sensor Networks (BSN'13), Boston, MA, May 2013.

Nabil Alshurafa, Wenyao Xu, **Jason J. Liu**, Ming-Chun Huang, Bobak Mortazavi, Christian Roberts, Majid Sarrafzadeh, "**Robust Human Intensity-Varying Activity Recognition using Stochastic Approximation in Wearable Sensors**", IEEE International Conference on Implantable and Wearable Body Sensor Networks (BSN'13), Boston, MA, May 2013.

Jason J. Liu, Wenyao Xu, Ming-Chun Huang, Nabil Alshurafa and Majid Sarrafzadeh, "**A Dense Pressure Sensitive Bedsheet Design for Unobtrusive Sleep Posture Monitoring**", IEEE International Conference on Pervasive Computing and Communication (PerCom'13), San Diego, CA, USA, March 2013.

Jason J. Liu, Cody Phillips and Kostas Daniilidis, "**Video-Based Localization Without 3D Mapping for the Visually Impaired**", 3rd Workshop on Computer Vision Applications for the Visually Impaired (CVAVI'10), Workshop of CVPR'10, San Francisco, June 2010.

CHAPTER 1

Introduction

The specific aim of this work is to investigate computational methods and algorithms that analyze pressure images of the body. However, it is useful to present the context of these methods as part of the larger application in the real world.

In healthcare, personal monitoring of one's health is an important goal. The application of state-of-the-art systems that relate to personal health monitoring have the goal of providing a 24/7 picture of one's health, namely "e-health". The key requirements of these systems is that they provide continuous available monitoring, must be as unobtrusive as possible, require as little human intervention as possible, identify and alert health risks, and be cost effective.

Firstly, Eysenbach [Eys01] defined e-health as:

> *An emerging field in the intersection of medical informatics, public health and business, referring to health services and information delivered or enhanced through the Internet and related technologies. In a broader sense, the term characterizes not only a technical development, but also a state-of-mind, a way of thinking, an attitude, and a commitment for networked, global thinking, to improve healthcare locally, regionally, and worldwide by using information and communication technology.*

This definition of e-health places the practice of healthcare in-line with the use of electronic systems that is not just limited to Internet technology. For example, e-health can mean the application of electronic health record systems in hospitals, i.e., hospital information systems (HIS), radiological information systems (RIS), picture archive and communications systems (PACS). It includes primary care office computerized systems, electronic prescriptions and order entry, and even email systems. Furthermore, telemedicine has been developed significantly such as in teleradiology and telepathology [KNP01], and now applications for remote vital signs monitoring are now seeing increasing favor.

Mark Weiser first coined the term ubiquitous computing and states the following at the beginning of his influential work [Wei99]:

> *The most profound technologies are those that disappear. They weave themselves into the fabric of everyday life until they are indistinguishable from it.*

His vision listed a number of properties which are summarized here. *Service is present everywhere.* This is the idea of ubiquity, meaning everywhere. A device can either be wearable, or other devices can be available wherever you go. *It is not the device but an environment.* It is not a single device, but a collection devices that work together to form a service and creates the system environment. *The user is not conscious of the device being used.* In contrast with smartphones or laptops that demand the attention of the user, ubiquitous computing devices work for the user in the background. The user, although aware that nearby devices exist, need not actively interact with the devices nor need to worry that the services of the devices are running.

> *Personal health monitoring strives for complete 24/7 coverage of well-being through the use of ubiquitous computing that focuses on e-health monitoring, diagnosis, alerting, and action.*

It is the round-the-clock environment of health management and technology utilization with as little human intervention as possible. Devices are required to be as unobtrusive as possible. This means that wireless solutions are preferable over wired solutions. Non-contact sensing is preferred over contact sensing. It is as if technology is not present at all, yet information is gathered and analysed, results concluded, and a plan of action advised. In general, no one system can provide complete 24 hour coverage, however, it would be desirable for anytime and anywhere health assurance.

1.1 Why is Personal Health Monitoring Important?

Healthcare costs are a major portion of the US gross domestic product, current estimates by OECD are approximately 17% of GDP [OEC12]. This is the highest in the world, most developed nations have their healthcare spending between 7 - 11% of GDP. Not only is the US healthcare spending at a very high level, it has been increasing since the beginning of the recorded data in 1960's. There are many reasons why this is so: the population is aging, utilization of health services is increasing, more advanced technology is used, labor resources are not increasing at the same rate as usage, insurance costs escalates with liability issues, and so healthcare is getting more expensive [SV09].

Chronic illness accounts for 78% of the total US healthcare spending [Com04]. From the 2004 US in-patient cost estimates on Medicare by the Agency for Health Quality Research, Healthcare Cost and Utilization Project, the five most costly of the chronic diseases in the US are: coronary artery disease ($39.6 billion), heart failure ($19.8 billion), mental health disorders ($11.4 billion), chronic obstructive pulmonary disease ($8.2 billion), and diabetes ($7.4 billion) [Com04]. These staggering amounts lead many to believe that much of the costs are preventable.

> *Approximately 95% of the $1.4 trillion that we spend as a nation on health goes to direct medical services, while approximately 5% is allocated to preventing disease and promoting health.* [DHH01]

The vast majority of the expenses are being incurred on prolonged hospital stays and managed care after which the chronic conditions have progressed past any turning point. Only 5% is spent on prevention. If many of these conditions are prevented earlier in the cycle by detecting occurrences of key indicators or proactively monitoring high risk patients, then a major portion of the healthcare costs will be eliminated. It is clear that chronic conditions currently are not being managed correctly. Even treatment at any earlier stage will reduce some of the costs.

Unfortunately, the current medical environment is one of reactive action and, in many cases, it is too late. By that point, the costs have escalated into the hundreds of thousands of dollars per patient [DDK09].

One solution is to provide as much out of hospital care as possible. This could be in the form of trained healthcare providers that operate outside of the hospital and are focused on personalized home-based care. Unfortunately this would not address the ever increasing health bill, since the current labor force would be stretched thin and in turn require more and more people to be trained in healthcare. By adding more people, the total expense for healthcare would increase.

The other and more reasonable solution would be to rely on technology. Technology can provide monitoring services not only within hospital environments but also at home. Current research has focused on many approaches to home-based remote monitoring. User initiated measurement devices such as weight scales and blood pressure monitors are one form of technology that have been wirelessly connected to monitoring systems. More ubiquitous systems such as those that are smartphone-based are also included in these solutions. These types of systems are not location dependent and professional medical help can be contacted when needed or, ideally, professional medical help will contact the patient when pending danger occurs.

Such personal health monitoring systems are complementary to the traditional forms of healthcare services and are not intended to replace them. The overall goal is to improve the quality of healthcare while reducing the costs. To this end, the strategy of moving the healthcare process toward the patient for in-home care, relying more on the patient's own personal needs and control, actually promotes active, healthy living style. In the end, personal monitoring improves the overall quality of life.

Not only are there cost benefits and reductions in the need for ongoing medical interventions, but also these continuous systems improve the compliance of medical condition management. It is estimated that up to $100 billion is wasted due to poor medical adherence [CAY06]. Continuous health management systems can address some of the problems with non-compliance. With automatic analysis tools, pertinent data can also be presented to the user about health issues. Furthermore, mobile communication with healthcare providers can provide current monitored data as well as important alerts.

So, the goals of personal health monitoring solutions are:

- Use ubiquitous technology for sensing, monitoring, analysing, and communicating to effectively manage healthy living.
- Be available 24/7.
- Be as unobtrusive as possible. Be as comfortable as possible.
- Require as little human intervention as possible.
- Identify important indicators of possible health risk.
- Provide information to the user or medical providers about health alerts.
- Be cost effective. Reduce costly and unnecessary medical services that are common with current healthcare practices.

1.2 What is the Impact?

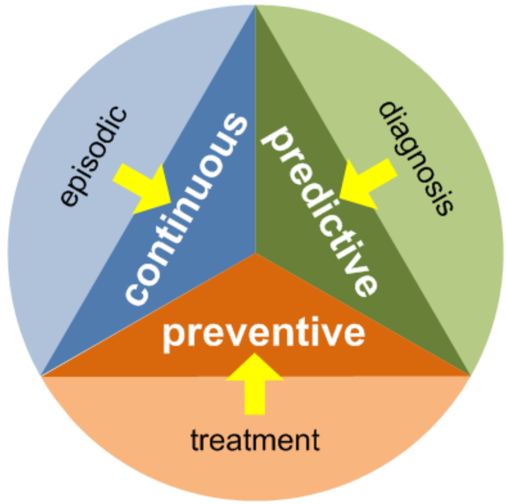

Figure 1.1: Transformation of Healthcare Environment.[1]

It is important to realize that the change to personal health monitoring is a cultural and sociological change. It requires a change in people's thinking, a change in one's idea of healthcare control, and a change in responsibility. The current landscape of healthcare has a limited supply of healthcare providers and they are burdened by the process of collecting information. It is a reactive environment in which action is taken after significant events occur. However, a shift in the process will allow physicians to concentrate on providing the medical expert care at the right time [SV09]. Continuous remote monitoring of the patient takes much of the load away from doctors. The focus toward patient monitoring will relieve much of the work of the healthcare professional. It requires a paradigm change toward user responsibility and pre-emptive action. Continuous and ubiquitous healthcare systems provides a promising answer to today's medical questions.

The impact of health monitoring is a three-fold transformation in the healthcare environment: (1) from episodic examination to continuous monitoring; (2) from disease diagnosis to disease prediction; (3) from reactive treatment to pre-

[1]courtesy of Wenyao Xu

emptive prevention. Figure 1.1 summarizes this change in healthcare. Currently, episodic patient examination only captures snapshots of the health status of individuals. Personal health monitoring aims for continuous coverage of healthcare. Currently, a disease is only diagnosed if a patient has a health complaint and makes a visit to a healthcare professional. The focus of healthcare change aims to move the analysis toward prediction. Once conditions have been diagnosed in patients, reactive treatment plans are prescribed. However, often this is too late. Pre-emptive prevention of medical conditions is the goal. There are existing steps toward pre-emptive prevention, such as early screenings for breast cancer and prostate cancer, however there is more that can be done.

1.3 Personal Health Monitoring Applications

In this section, a selection of medical applications are introduced where continuous monitoring systems will affect the change toward better human health. There are many more applications that will see huge benefits that are not described here. Figure 1.2 shows four applications that have seen promising system developments: Pressure Ulcer prevention, Cardiopulmonary monitoring, Fall prevention, and applications in rehabilitation.

Within each application, there could be a number of systems that work together to provide complete coverage. Each of the systems can be broadly categorized [OGF08] into:

- Mobile devices: devices that are portable such as mobile phones, smart phones, tablets, PDAs, and even laptops.
- Wearable items: devices that can be a part of clothing or e-textile, or devices that are strapped to the body.
- Stationary devices: devices such as sensors embedded or mounted in furni-

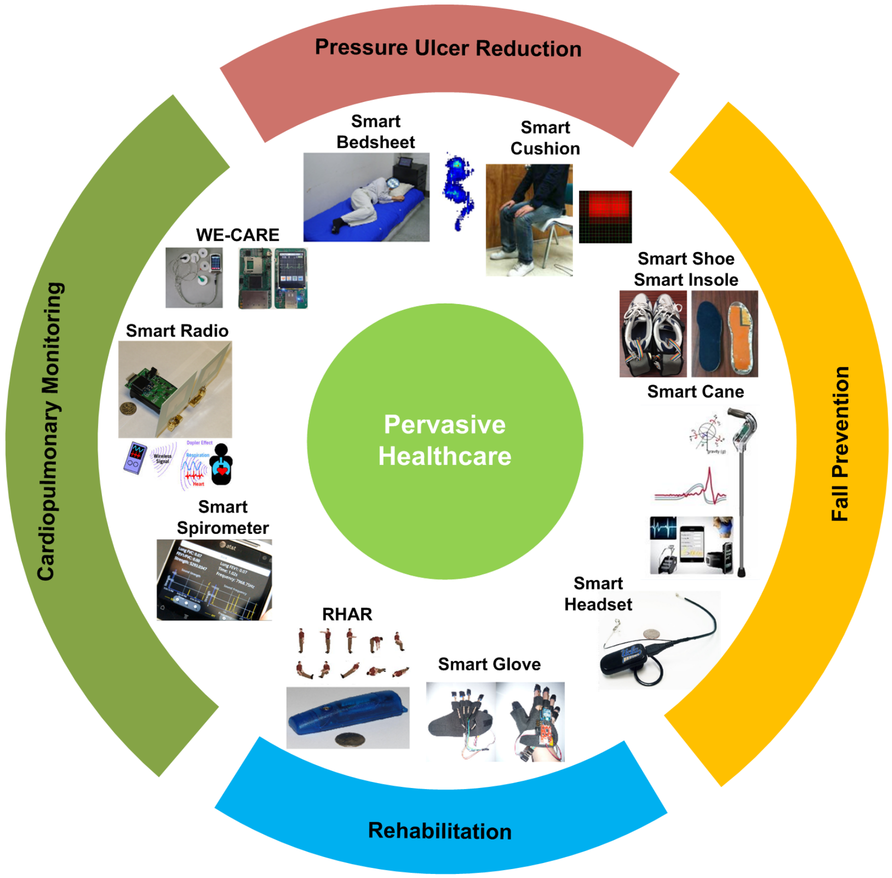

Figure 1.2: Applications of Personal Health Monitoring.[2]

ture, building walls, or fixed structures.

Although there has been a lot of development and good applications for implantable devices, such as pacemakers, defibrillators, diabetic implants, such devices shall not be included in this work due to their invasiveness.

The following subsections introduce some of the current development as well as relevant applications for the technology. The applications of pressure ulcer prevention and physical rehabilitation motivates the computational methods proposed in this work and will be the focus of the subsequent dissertation. The remaining applications, and there are many more not discussed here, highlight other opportunities for healthcare improvement.

[2]courtesy of Wenyao Xu

1.3.1 Pressure Ulcer Prevention

One of the main problems for post-surgical patients and elderly patients is formation of pressure ulcers [PHR98]. Pressure ulcers, or bedsores, are localized injury to body tissue, usually near the bone, resulting from low blood circulation and lack of movement. Hospital staff need to be attentive to subjects that are more susceptible to this condition, and take action to relieve pressure on the highly sensitive locations by changing their sleep postures. Current best practices in nursing involve moving patients every several hours. However, there is no guarantee that patients remain in one posture in the meantime.

A pressure-sensitive bedsheet system provides an unobtrusive method for sleep posture monitoring and sleep analysis [LXH13]. The magnitude of the pressure need not be high, but the duration of pressure is critical. A desired system would use technology to measure how long a patient is lying in one particular posture and automatically create notifications that an intervention is required. A method to recognize sleep postures is detailed in Chapter 3. This method extracts geometrically meaningful features and applies a classifier that uses sparse representation.

Figure 1.3: Smart Bedsheet

The goal of any medical system that prevents the formation of pressure ulcers requires the analysis of sleeping postures, as well as notifications of susceptible and impending pressure points on the patient's body. Chapter 4 presents methods to locate specific bodyparts that are susceptible to pressure ulcers.

1.3.2 Respiration Rate Monitoring

As the best way to heal the human body and recover energy, sleep has many implications on our overall health. It has been widely used as a diagnostic indicator in diverse medical applications. For example, sleep stage is a proven biometric in diagnosing cardiovascular disease, diabetes and obesity [Par09]. Sleep difficulty is associated with psychiatric disorders such as depression, alcoholism and bipolar disorder [Tha06].

There have been several research works on sleep apnea analysis with sleep postures in recent years. Lee et al. reported that lateral (lying on side) postures can reduce sleep disorders for mild and moderate sleep apnea patients [LPH09]. Ambrogio et al. discovered the relationship between sleep postures and chronic respiratory insufficiency, which leads directly to sleep apnea [ALK]. Oksenberg and Silverberg investigated breathing disorder and sleep postures [OS06]. They suggested that patients with obstructive sleep apnea should avoid sleep in the supine (lying on back) position.

Respiratory rate is not only important for detecting disorders such as sleep apnea or suddent infant death syndrome, but also a predictor of the onset of cardiac arrest. There have been many studies that show the high respiratory rates are good indicators of cardiac arrests: Fieselmann et al. [PKO03] and Goldhill et al. [RM11] observed a high proportion of cardiac arrest when respiration rate exceeded 27 and 25 breaths per minute respectively. Furthermore, mortality rate increased with respiratory rate [RM11]. Variance in respiratory rate is also a stronger predictor of cardiac problems compared to variance in heart rate or blood pressure [HKV02].

Chapter 4 includes a method to identify the respiration centric bodyparts, i.e., the chest and torso. It shows that by localizing on the correct portion of the body, respiration accuracy is improved.

1.3.3 Rehabillitation

Another application that uses the same pressure sensitive bedsheet is on-bed physical rehabilitation (Figure 1.4) for those who are recovering from surgery or for the bed ridden. Physical rehabilitation is a proven method that has been well documented to provide lasting benefits to patients [BH07, FCE01]. For example, Johns Hopkins Hospital has reported up to 22% reduction in ICU length of stays and reductions in net financial costs due specifically to the inclusion of early physical rehabilitation programs [LMK13]. Patients undergoing physical rehabilitation follow the exercises assigned by the physical therapist on a regular or semi-regular basis. A physical therapist needs to manually monitor and evaluate the rehabilitation process to check that the progress of the patient goes according to expectation. As a result, the cost of monitoring rehabilitative exercises is large and the recovery progress of each patient is difficult to quantize.

Figure 1.4: On-bed Rehabilitation

A method in Chapter 5 analyzes the dynamic progression of pressure image sequences using manifold learning. The image sequences are reduced to a low dimensional subspace that can be measured against expected prior data for each of the rehabilitation exercises. A metric to compare manifold similarities is also described and can accurately track compliance of patients to prescribed treatment programs. It allows physical therapists to evaluate how well patients adhere to the rehabilitation exercise.

1.3.4 Fall Risk and Prevention

Annually, 1.8 million older adults are treated for falls, which resulted in $20 billion in direct costs in 2008 [CDC, SCF06]. A lightweight smart shoe and supporting infrastructure has been developed for gait and human balance monitoring. This system comprised accelerometers, compass, and pressure sensors mounted within shoe insoles with built-in Bluetooth communication to cell phones [NAH10, XHA12]. This system monitored walking behavior and used instability assessment to classify various types of activity. An important application of this technology is to determine fall risk and identification of episodes as precursors to instability. For mainstream use, the cost of smart insoles needs to be viable; currently, the estimated manufacturing cost is under $200 with further research being continued.

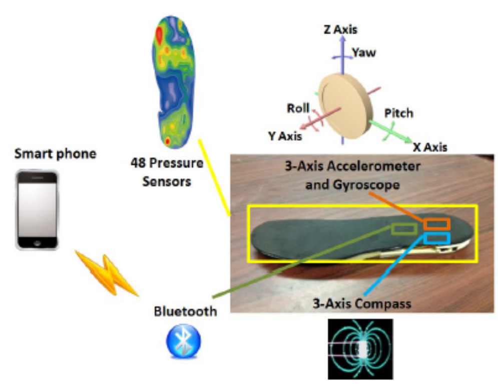

Figure 1.5: Smart Insole

For applications, such as activity monitoring, the smart insole captures a record of a person's activity. This is beneficial for obesity analysis and general fitness. Other applications are pressure ulcers that develop especially for diabetics. The smart insole can analyse the pressure distribution of a person's foot and generate alerts for prolonged pressure points.

1.4 Summary of Contributions

There are a variety of commercially available pressure sensing systems for measuring body pressure [Tek, Xse, Vis]. Although these systems provide high resolution and accurate pressure scans, the costs are expensive. This work employs a low cost, eTextile bedsheet that is comfortable and unobtrusive.

The contributions in this work are summarized:

- A framework is proposed for automatic sleep posture analysis based on a dense pressure sensitive bedsheet prototype (64 $\times$ 128 sensors) designed using e-textile material. In many cases, pressure image analysis is more challenging than video image analysis due to incomplete body pressure maps and self occlusions.
- A set of geometric features from pressure images is designed for posture analysis. These features are effective not only in distinguishing different postures but also in characterizing each posture with physical meanings.
- A method of classification based on sparse representation is employed to recognize sleep postures. In addition, a set of three heuristics based on sparse representation is proposed to classify sleep postures.
- A framework is proposed to localize key bodyparts within a pressure distribution image by defining a pictorial model of the human body.
- A refinement of bodyparts localization is presented to improve respiration monitoring using the pressure sensitive bedsheet.

- A framework is proposed to recognize pre-defined body motions on the bedsheet for the purpose of physical rehabilitation monitoring. This method uses manifold learning to reduce the dimensionality of the feature space so that a visual representation of motions can be compared.

- A theoretical investigation of sensor sample reduction is presented that allows images from the bedsheet to be reconstructed accurately from a minimal set of data points.

1.5 Dissertation Organization

In all, this work presents computational methods for analysis of pressure images from a pressure sensitive bedsheet. Chapter 2 introduces the physical hardware of the bedsheet that includes the pressure sensitive material and the scanning system to extract the pressure values. The following chapters describe several methods of analysis. The first method is static body posture recognition (Chapter 3). The second method describes methods for fine-grain bodypart identification (Chapter 4). This is used for applications in respiration monitoring as well as pressure ulcer accumulation risk.

Chapter 5 presents on-bed dynamic motion recognition in the context of physical rehabilitation exercise detection.

Then Chapter 6 presents a sensing strategy for the bedsheet. Currently, all pixels are scanned to compose the pressure image. However, a question is asked whether a full resolution pressure image is required to classify postures or locate bodyparts? This chapter looks at possibilities of reducing the density of samples in order to accurately reconstruct a full size pressure image without losing classification accuracy.

CHAPTER 2

A Dense Pressure Sensitive Bedsheet

This chapter describes the design of the pressure sensitive bedsheet. The bedsheet comprises eTextile which is a fabric that has resistive properties. The fabric is arranged such that pressure values can be determined from points across the sheet. The method of scanning the array structure is also described in this chapter.

The bedsheet system is designed with the following consideration:

- High-resolution: The bedsheet should offer high resolution for pressure sensing. Given enough resolution, it is possible to quantify the applied pressure on body parts and enable high accuracy medical diagnosis.
- Comfort: The user should feel comfortable lying on the sheet. Also, it should be easy to deploy in the home or hospital.
- Low-cost: For widespread use, the cost for the bedsheet implementation should be low and affordable for most people.

There are some existing sensor products [Xse, Vis] comprised of many piezoelectrical pressure sensors. However, none of them meets the above design criterions for wide applications.

2.1 eTextile Sensor Array Architecture

eTextile is a fiber-based fabric that is coated with piezoelectric polymer. The basis of this bedsheet design is described in the related work [XLH11]. Initially, the electrical resistance between the top and bottom surfaces is high. When compression force is applied to the surfaces of the eTextile, the inner fibers are squeezed together and the resistance reduces. Because of this characteristic of eTextile, a high-density pressure sensor array can be designed.

In traditional sensor arrays, each location has its own independent sensor, complete with its own analog to digital converter (ADC). So, to build a $M \times N$ sensor array, MN sensors are required, and MN I/O pins are required. With a desired high resolution pressure image of around 8,000 pixels, this sort of architecture is not appropriate.

Figure 2.1: The structure of textile sensor and sensor array design

Instead, a three layer sandwich structure is used to build this sensors with sequentially controlled scanning. The top layer of the system is regular fabric that is coated with parallel conductive lines. The middle layer is the eTextile. The bottom layer is the same as the top layer but arranged perpendicularly, so that the conductive lines form a grid pattern (See Figure 2.1. The area where the lines intersect form a pressure sensitive resistor. The total thickness of the three layers is approximately 1.5mm, and makes the sheet flexible, thin and comfortable enough for unobtrusive monitoring. Moreover, the $M \times N$ sensor structure only requires $M + N$ I/O pins.

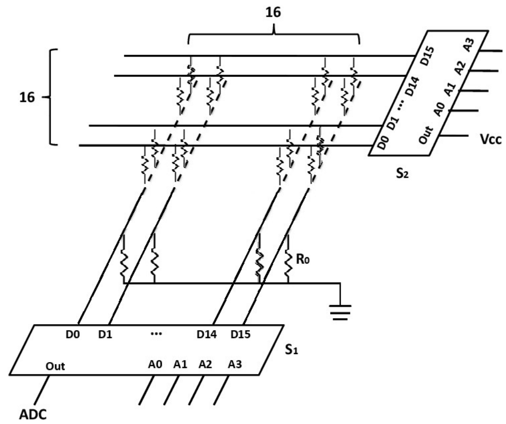

Figure 2.2: The peripheral circuit for sensor array scanning

2.2 Scanning Method

The sensor structure is scanned in the following way (Refer to Figure 2.2). Each conductive bus on the bottom is connected to ground via an offset resistor R_0. Two analog switch modules, S_1 and S_2, are used and are controlled by a microcontroller. Each conductive bus on the top is connected to a voltage supply via analog switch model S_2. The microcontroller activates the supply to each line individually in sequence. With this voltage applied to the one of the top lines, there is an electric circuit from the top line, through the resistive eTextile, along the bottom bus lines to ground via the offset resistors. There is a voltage drop across the offset resistors according to their resistance and the resistance of the eTextile. They are essentially voltage dividers. The voltage is measured by the switch module S_1 in sequence. Both switches S_1 and S_2 are used together to determine which sensor is selected. For example, when S_2 connects bus i on the top layer to a voltage supply and S_1 reads the voltage at bus j, the ADC will read the sensor located in row i, column j, which is denoted as V_{ij}. In summary, this peripheral circuit has random accessability for an arbitrary sensor in the system.

Figure 2.3(a) shows an example of a user lying on the bedsheet. The subject sleeps on the bedsheet in a right fetus posture, and the corresponding pressure image is illustrated in Figure 2.3(b). In the pressure image, body parts (such as hip, legs) can be seen although perhaps not clearly in many cases.

(a) One subject on the bedsheet system (b) Pressure image

Figure 2.3: System demonstration with one subject sleeping in a right fetus posture.

2.3 Hardware Build

A prototype of the bedsheet was built, containing 64×128 pressure sensors, with total size of 1.25m $\times$ 2.5m. The 64 column conductive lines and 128 row conductive lines generated 8192 joint intersections. A sampling unit was connected to all conductive lines and performed matrix scanning to measure pressure map sequences. Retrieved pressure map signals of the 8192 sensors are quantified to 8 bit integers with values ranging from 0 to 255. In fact, 0 represents the highest e-textile resistance/no pressure detected and 255 representing lowest e-textile resistance/maximum detectable pressure value. The sampling rate is adjustable up to 10Hz. 1.5Hz is sufficient for posture detection and respiration rate detection, while 5Hz is suitable for physical rehabilitation exercise recognition.

This system was capable of recording pressure data acquired from the pressure sensitive bed sheet over time into a log file. An application was implemented on a tablet and stored all pressure images for further analysis. The current system stores the data as comma separated files (CSV file) which can then be imported into MATLAB as a three dimensional matrix (frame number, row and column) for post-analysis.

CHAPTER 3

Static Body Posture Recognition

3.1 Background

To date, researchers have proposed different ways to monitor sleep posture automatically. Video cameras and microphones have been used previously to study sleep posture patterns. For example, Nakajima et al. [NMT] prototyped a system based on visual signals to analyze sleep posture changes. However, lighting issues are a main drawback of using video. Low light levels at night add noise to the images, and even when near-infrared cameras are used [LY08] the images still produced non-uniformity and artifacts. Furthermore, video and voice recording raise serious privacy concerns for users.

Inertial sensors, including accelerometers, gyroscopes and magnetometers, are another applied technique used to monitor sleep. Sadeh and Acebo attached several tri-axial accelerometers on limbs of people to monitor sleep patterns via actigraph [SA02]. Kishimoto et al. deployed 14 wearable motion sensors on users at home for remote sleep posture analysis [KAO06]. The main downside to this technique is that sensors have to be attached to the body which can be uncomfortable or burdensome to the users. Recent work with ECG measurements has shown that the morphology of the human QRS complex can be used to estimate body posture [LHL13].

Alternatively, dispersed pressure sensors embedded in the mattress can record when changes in body posture occur. This method is unobtrusive and does not interfere in the comfort of users. Also it is a stable medium that is not affected by changes in the environment. Hoque et al. facilitated a mattress with wireless-powered accelerometers to record movement activity [HDS10]. Jones et al. developed a bedsheet system with 24 pressure sensors [JGK06]. However, such prior work focused on detecting posture change rather than recognizing body posture. Similarly, Foubert et al. were able to detect changes from lying to sitting posture [FMG12]. Mattress indentation is another modality to assess sleeping patterns [VHW11].

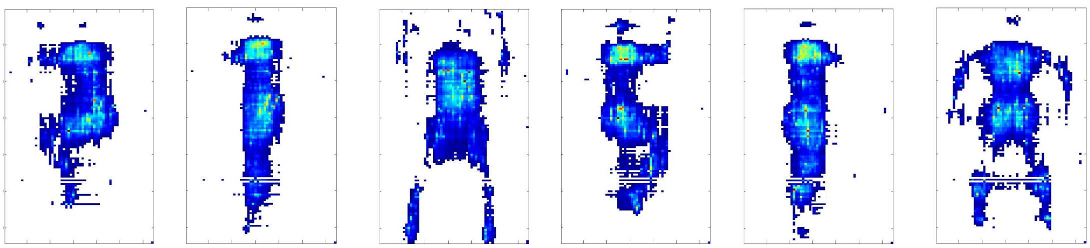

Figure 3.1: Human Body Pressure Image Samples

This chapter focuses on sleep posture analysis using pressure sensors. A dense pressure sensitive textile bedsheet and pressure image analysis is employed for sleep posture recognition. The proposed methods are evaluated with 14 subjects for 6 common sleep postures in static trials. Furthermore, 8 hour continuous monitoring trials are also presented. The proposed method exhibits better performance in terms of accuracy and robustness than traditional classification methods.

In contrast to previous work which have generally focused on recognizing three postures, Left Fetus, Right Fetus, and Supine postures [HLA09, NAZ10], this work describes a classification system that includes additional more complex but common postures: Left Log, Right Log, and Prone. The log postures are positions where subjects are lying on their sides with legs almost straight. In many hospital settings, these postures are supported with pillows behind their shoulders and back. The aim of such postures is to ameliorate the possibility of developing pressure ulcers on the hips, shoulders, and buttocks.

3.2 Framework for Sleep Posture Analysis

Figure 3.2 shows the sleep posture analysis process. The central three steps, Pre-processing, Feature Extraction, and Sparse Classification will be discussed in this section.

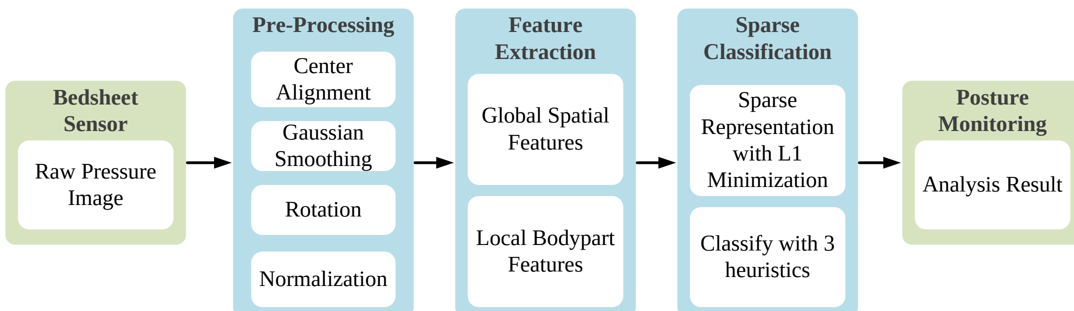

Figure 3.2: Sleep Posture Recognition Framework

3.2.1 Pre-processing

The pre-processing on the raw pressure images is required so that the images can be standardized in such a way as to enable successful classification. The raw images contain noise and artifacts that affect classification, and pre-processing mitigates these side effects as much as possible.

- The subject can be located anywhere on the bedsheet, so to correct this, the images are aligned to a common center of mass and relocated to the center of the image.
- A smoothing filter of a symmetric 5×5 unit normal distribution is applied. This smoothing minimizes the effect of noise in the pressure map.

- The images are rotated so that the dominant axis of the body shape is aligned vertically in the image. The dominant axis is found by an eigenvector calculation by approximating the human body geometry as an ellipse. This accounts for the different lying angles for the subjects.

- The images are normalized so that the sum of pixel weights is one. This step attempts to counteract the effects of different body mass of patients.

3.2.2 Feature Extraction

Traditional feature extraction methods on images include dimension reduction techniques. Widely popular is Principal Component Analysis [Jol] which relies on finding the dominant orthogonal axes which maximizes the statistical variances in the data. PCA is largely data dependent and is a general method to find macro structure in datasets. This method has been applied to sleep posture recognition in current literature [YOF11].

In this work, a different method of feature extraction for posture classification is proposed, one which is based on the geometry of the pressure images. It is more attuned to the physical characteristics of the body shape and has a definite physical meaning. An advantage of using these proposed features over PCA reduction is the processing time required to extract these features; the proposed features are based on simple geometry.

In all, 32 features are extracted from each of the pressure images. The features are described as either Spatial features or Bodypart features. Spatial features are those features that describe global aspects of the image such as the proportion of the image that is covered by the subject, the symmetry of the image, and direction of any curvature in the pressure image. Bodypart features are localized features that describe location and size of expected body parts such as the hip and shoulder.

Table 3.1: Global Spatial Features

No.	Name	Description
1	Coverage	Proportion of image covered
2	Per25	Coverage of 25% of pressure
3	Per50	Coverage of 50% of pressure
4	Per75	Coverage of 75% of pressure
5-12	Reg1 - Reg8	Coverage over 8 fixed rectangular regions
13	Symmetry	Measure of pressure symmetry
14	Balance	Measure of pressure on both sides of image
15	DirCurve	Measure of curvature of pressure image

Refer to Table 3.1 for a full a listing of the global Spatial features and Table 3.2 for the localized Bodypart features. A more detailed explanation of the features follows here. Unless otherwise stated, it is assumed that the x axis is along the short side of the bedsheet, the y axis runs along the long side of the bedsheet.

Coverage Features (1-12)

The first feature is Coverage, which is the number of pixels that have non-negative sensor values divided by the total number of pixels. The next 3 features consider coverage for the pixels that contain 25%, 50%, 75% of the total pressure. Features 5-12 relate to coverage by regions. The regions are 8 equally sized subdivisions of the image as shown in Figure 3.3. Given that the original dimensions of the image are 64×128 pixels, the region sizes are 32×32 pixels.

Symmetry and Balance (13, 14)

Symmetry is the sum of the absolute value of the difference of pixels on either side of the center image line. A supine posture would have more symmetry than a side posture. Balance is the sum of the difference of pixels on either side of the

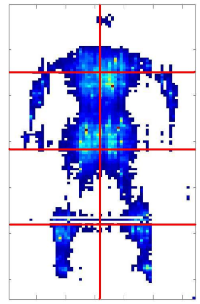

Figure 3.3: Coverage by Regions: Features 5-12

center image line. This is different to the Symmetry measure in that it does not take the absolute value of the difference of pixels into consideration. The resulting measure describes which side of the image contains most of the pressure.

Direction of Curvature (15)

This measure detects the dominant direction of curvature of the body image. A person lying on one side will have a detected body curvature, whereas a supine position should exhibit a straighter pressure image. The steps to extract this feature metric are as follows:

- Create a binary image that contain pixels that are above a suitable threshold. The choice of threshold is obtained experimentally, although a reasonable estimate is 50% of the peak sensor value.
- Skeletonize the binary image by finding midpoints of boundary pixels (see Figure 3.4).
- Remove joint pixels from the skeleton so that each curve is separated. Remove curves that are shorter than 5 pixels.
- For all pixels along the curve, find the angle bisector. The director of curvature is taken as the sum of the y components of the angle bisectors, i.e., in the lateral axis of the bedsheet.

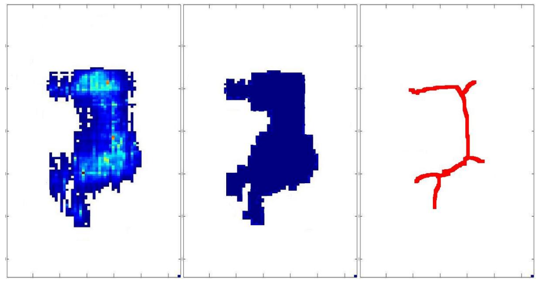

Figure 3.4: Direction of Curvature feature: Left: original image. Middle: thresholded image. Right: skeletonized image.

Table 3.2: Local Geometrical Bodypart Features

No.	Name	Description
16,17	HipPoint	(x, y) location of hip location
18-21	HipBox	(x, y, width, height) of bounding box of hip
22	HipArea	Area in pixels of bounding box of hip
23	HipPtoBox	Ratio of hip location to bounding box width
24,25	ShPoint	(x, y) location of shoulder location
26-29	ShBox	(x,y,width,height) of bounding box of shoulder
30	ShArea	Area in pixels of bounding box of shoulder
31	ShPtoBox	Ratio of shoulder location to box width
32	HipShDist	Hip to shoulder distance

Hip Features (16-23)

Since pre-processing of the image is done initially, the assumption is made that the hip is located in the quarter of the image below the center of mass of the pressure image. An estimate of the hip location is taken to be the pixel that is located at the weighted center of pixels in this quarter image. The bounding box around the hip is the rectangular region of the pixels that contain 75% of the pressure values within the quarter image below the center of mass of the pressure image. The ratio of hip location to bounding box width provides a measure that shows where the hip location is in relation to the bounding box of the hip.

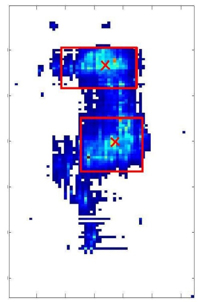

Figure 3.5: Hip and Shoulder Features

Shoulder Features (24-31)
Similar to the hip features (16-23) above, the same information is extracted for the shoulder. A similar assumption applies to the quarter image above the center of mass for the shoulder location. Figure 3.5 shows a sample of the locations and bounding boxes of the hip and shoulders. Finally, Feature 32 is the pixel distance between hip and shoulder locations.

As all the features described above are on different scales, the feature values are scaled and shifted so that the resulting values are in the range [0,+1].

3.2.3 Classification Preliminaries

Before the investigation of Sparse Classifiers, it is useful to review the progression of classification basics from Nearest Neighbor to Nearest Subspace, then to Sparse Classification.

The Nearest Neighbor classifier simply finds the closest training sample in the feature space to provide a prediction for a test sample. Euclidean distance is the most common measure of closeness between the test sample and the training samples given that the feature space consists of continuous variables.

With a training data set of n samples, and each training sample having m dimensions (features), let each sample be $a_i \in R^m$. Now given a new test sample $y \in R^m$, the nearest neighbor is the training sample that minimizes the distance to the test sample:

$$\arg\min_i ||y - a_i x||_2 \tag{3.1}$$

where x is an identity vector and it is assumed that all features have been scaled to a common range. The prediction is the class to which the nearest sample belongs.

Nearest neighbor classifier is a popular classifier because of its simplicity and robustness to noise as long as there is sufficient training data. However it has several disadvantages such as high dimensional data reducing the effectiveness of classification. Some features (dimensions) may be more important than others in classification and Nearest Neighbor does not take this into account.

The Nearest Subspace classifier [LGL] extends Nearest Neighbor to include information about assigned class labels. Instead of finding the closest training sample, Nearest Subspace finds the closest subspace that is spanned by training samples belonging to that class. So given a training data set of n samples, and each training sample having m dimensions (features) and having a class label k, let the training samples for class k be A^k. The training samples are column vectors placed side by side. Now given a new test sample $y \in R^m$, the nearest subspace is the class that minimizes the distance of y to the subspace spanned by all the training samples of that class:

$$\arg\min_k ||y - A^k x||_2 \tag{3.2}$$

where x is a vector of weight coefficients. For each class k, the test sample y can be represented by a weighted combination of the training samples in class k if one considers each of the training samples as basis vectors in the subspace spanned by the training samples. So for each class k, $A^k x$ represents a reconstructed sample similar to y. This classifier assigns the class label that minimizes the reconstruction error. The solution to Nearest Subspace can be found using convex optimization with the constraint that all weights are non-negative. Without this constraint, the solution degenerates in this overdetermined system.

The Nearest Subspace classifier finds a representation of a test sample in the subspaces spanned by class training samples. This idea is extended further using Sparse Representation. The general idea is to represent the test sample using all the training samples, initially without regard to the classes of the training samples. By imposing sparsity constraints on the representation of the sample, a different type of classifier can result. The following section describes classification using Sparse Representation of samples.

3.2.4 Classification using Sparse Representation

Sparse Classification has been used previously in other medical analysis and has been shown to have effective performance over a wide range of applications [XZS12]. The classification method comes from the theory of Compressed Sensing [CRT06], which proposes that data exhibits sparsity in some transformed representations. That is, a signal can be represented as a sparse signal in a transformed feature space, and can be accurately re-constructed with a lower sampling rate than the Nyquist-Shannon rate.

Given a data set of n samples, with each sample having m dimensions (features), define the data matrix $A \in R^{m\times n}$ that comprises these m-element column vectors arranged side by side. Now given a new sample $y \in R^m$, can a solution $x \in R^n$ be found such that x is described in terms of the data set? i.e., can one find x that satisfies:

$$y = Ax. \tag{3.3}$$

So y is a linear combination of the columns in the data set, and $x = [x_1, x_2, ..., x_n]^T$ is an unknown vector of coefficients. This linear system is underdetermined when there are more unknowns than equations, and hence there are infinitely many solutions for x. This is the case for the formulation of posture classification in this work. However, if certain constraints are imposed, then a unique solution for x exists and will accurately represent the original sample. There are 3 main sparsity constraints on x that have been considered in literature.

- l_0 sparsity is defined to minimize the number of non-zero elements of x. Solving for x has been shown to be NP-hard [Nat95].
- l_2 sparsity is the efficient least squares solution, however this is not always equivalent to the l_0 solution.
- l_1 sparsity is defined as the minimal sum of absolute values of elements of x. Candes et al. [CRT06] have proved that l_1 sparsity is equivalent to l_0 and, moreover, can be solved as a convex optimization problem:

$$\begin{aligned} \hat{x} &= \arg\min_x ||x||_1, \\ s.t. \quad y &= Ax. \end{aligned} \tag{3.4}$$

The sparse representation of a sample is used in classification by matching this representation to a set of class labels. The data set A comprises training samples and each sample has been assigned a class label, C_n. Let each training sample be represented as a column vector, a_{ij}, where j is the sample number within class i. The number of samples need not be the same for each class. The data matrix A is shown here with samples grouped together in their classes:

$$A = \Bigg[\underbrace{\begin{matrix} | & | & \\ a_{11} & a_{12} & \dots \\ | & | & \end{matrix}}_{class1} \; \underbrace{\begin{matrix} | & | & \\ a_{21} & a_{22} & \dots \\ | & | & \end{matrix}}_{class2} \dots \underbrace{\begin{matrix} | & | & \\ a_{k1} & a_{k2} & \dots \\ | & | & \end{matrix}}_{classk} \Bigg].$$

Any test sample y is represented by a linear combination of the training samples:

$$y = a_{11}x_1 + a_{12}x_2 + \cdots + a_{kj}x_n, \tag{3.5}$$

where k is the number of class labels and j is the number of training samples for the k-th class.

The l_0 minimized sparse solution for x will have only a small number of non-zero elements. The training samples that correspond to the non-zero elements are those that can represent the new sample well. 3 heuristics are proposed to select the class label given a sparse solution for x and the data set with training labels as follows.

- Maximum Coefficient (MC). The class label belonging to the training sample that corresponds to the largest coefficient of the sparse solution of x is the predicted class label:

$$\hat{k} = C_{\arg\max_i(x_i)}. \tag{3.6}$$

- Maximum Sum of Class Coefficients (MSCC). The predicted class label is the class whose sum of coefficients of x is maximized:

$$\hat{k} = \arg\max_k(\sum_{i \in a_{ki}} x_i). \tag{3.7}$$

  In other words, for each class k, take the sum of the coefficients of x that correspond to the training samples belonging to that class. The predicted label is the class that maximizes these sums. The training samples that are most closely represented to the test sample should correspond to the bulk of elements of the sparse solution to x.

- Minimum Class Residual (MCR). An alternate choice for a heuristic to predict the class label is to find the class that minimizes the class residual. The residual is the error between the test sample and the reconstructed sample based on the sparse solution to x:

$$residual = ||y - A\hat{x}||_2. \tag{3.8}$$

So the predicted class is

$$\hat{k} = \arg\min_{k} ||y - A_{ki}x_i||_2. \tag{3.9}$$

Each of these 3 heuristics are evaluated in Section 6.5.3.

3.2.5 Hidden Markov Model for Continuous Posture Evaluation

In experiments on the continuous sleep posture monitoring, an investigation of the use of Hidden Markov Models [Rab89, QB08] on time sequential images is performed. The Hidden Markov Model (HMM) is a stochastic process where internal states of a system depend only on previous states and are hidden from direct observation. In this application, the hidden states are the sleep postures of the subjects and the direct observations are the pressure images from the bedsheet. Using HMMs, the sequence of postures is ascertained from the sequence of pressure images and knowledge of the state transition and observation probabilities.

The formulation of an HMM is as follows (refer also to Figure 3.6). The N postures are represented as N hidden states, $\{S_1, S_2, \ldots S_N\}$. Postures can change to another posture according to an assigned transition probability a_{ij}:

$$a_{ij} = Pr(s_{t+1} = S_j \mid s_t = S_i), \tag{3.10}$$

where s_t is the posture at time t. So a_{ij} is the probability that a subject who is currently sleeping in posture i changes to posture j. Sleeping postures can remain in one state for an indeterminate amount of time, i.e., the current state can transition to the same state, and this allows time-scale invariance in this model. With N postures, there are $N \times N$ transition probabilities. In the experiments in Section 6.5.3, the state transition probabilities for each subject are calculated from the training data.

Although the direct observable outputs from this system are the pressure images, the classification method is carried out on each image to produce predictions for postures. So for each state S_i, there is the probability b_{iq} that posture q is predicted. Let v_q be the predicted posture, then the observation probability, b_{iq}, is the probability of predicting posture v_q given the hidden posture is S_i:

$$b_{iq} = Pr(v_q \mid s_t = S_i). \tag{3.11}$$

So, for every observed pressure image at time t, the HMM calculates all the observation probabilities for the N predicted postures. The actual probability calculation is based on a confidence measure from each of the heuristics of the Sparse Classifier.

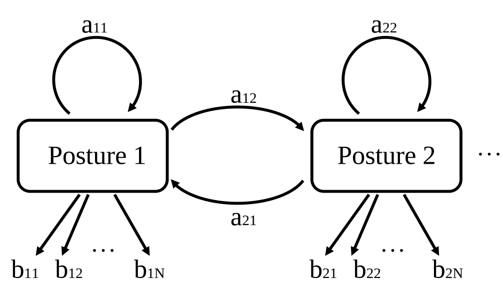

Figure 3.6: Hidden Markov Model with hidden postures. Only 2 postures are shown in this diagram.

The proposed confidence measure is a relationship between first best match and second best match from a different posture [Low04]. For example, the Maximum Coefficient (MC) heuristic finds the posture that corresponds to the training sample with the largest coefficient of the sparse solution. Let the maximum coefficient for this predicted posture v_q be m_1. Let the second best coefficient of the sparse solution that does not have the same predicted posture v_q be m_2. Then the observation probability can be calculated as:

$$\frac{m_1}{m_1 + m_2}. \tag{3.12}$$

As the solution of the coefficients is sparse, most of the observation probabilities are zero. The observation probability for the Maximum Sum of Class Coefficients (MSCC) heuristic is similar where the first best match m_1 is the maximum sum of the class coefficients and the second best match m_2 is the next best sum of the class coefficients of a different class. The Minimum Class Residual (MCR) is adjusted to account for the minimization:

$$1 - \frac{m_1}{m_1 + m_2}, \tag{3.13}$$

where m_1 is the minimum class residual and m_2 is the residual for the next best class. The HMM results for the confidence measures for the 3 heuristics are presented in Section 3.3.3.

3.3 Experimental Results

3.3.1 Experimental Setup

Two sets of studies in the lab evaluate the performance of the system for sleep posture monitoring. The first study was designed to collect training data and to evaluate short term performance over fixed intervals. The second study analysed the performance of the system for overnight continuous monitoring. The results of the second study is given in Subsection 3.3.3.

This section describes the performance of the first study. There are 14 subjects in the experiment, where 9 subjects are male and 5 subjects are female. The weight of the subjects ranges from 55kg to 85kg, and height between 155cm and 185cm, as shown in Table 3.3. The bedsheet system was deployed on a standard twin-size coil spring mattress during the experiments.

In Idzikowski's study of 1000 people [Idz03], left and right fetus postures, i.e., with legs bent, are most common at 41%. The other side lying postures, i.e., with straight legs, account for 28% of positions. These are referred to as log postures.

Table 3.3: Training subjects

	Gender	Age	Weight (kg)	Height (cm)
1	Female	25	57	158
2	Female	31	53	162
3	Female	27	65	168
4	Female	24	58	162
5	Female	23	60	165
6	Male	27	70	178
7	Male	26	74	172
8	Male	22	62	170
9	Male	35	70	180
10	Male	39	66	178
11	Male	28	72	184
12	Male	27	68	175
13	Male	29	63	173
14	Male	26	65	176

Supine (8%) and prone (7%) postures are the next most common. Therefore, for the experimental evaluation, the 6 postures including Left-Log (LL), Left-Fetus (LF), Right-Log (RL), Right-Fetus (RF), Prone (P) and Supine (S) are investigated. The examples of these postures are shown in Figure 5.5.

In the data collection, 40 samples were recorded for each of the 6 postures for each subject. At fixed intervals, the pressure image of the subject's posture was recorded while the subject maintained a comfortable sleeping position. Variations in body, arm and leg positions were allowed and the system is tested on a range of positions that fall within the 6 defined postures. All postures include a standard queen size pillow for the head. Testing was carried out with Leave One Out Cross Validation by subject, i.e., test on one subject's data with the training data

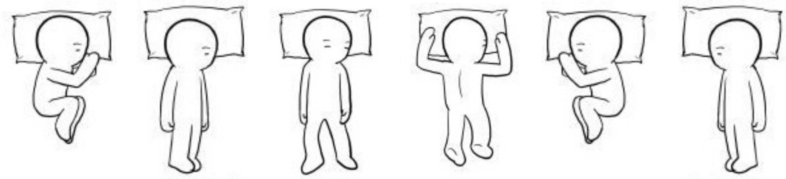

(a) Right Fetus (b) Right Log (c) Supine (d) Prone (e) Left Fetus (f) Left Log

Figure 3.7: Six Postures used in experiments.

from all the other subjects. Repeat this for each subject. Sparse classifiers are implemented using the CVX convex optimization package [CVX12].

The time to process each image using this method is 0.21s on a single core 3.0Ghz processor, of which 0.012s is used to extract the geometric features. Given that posture does not change much while sleeping, this timing is sufficient for this application and can be implemented within an embedded microprocessor.

(a) Camera frame for overhead recording

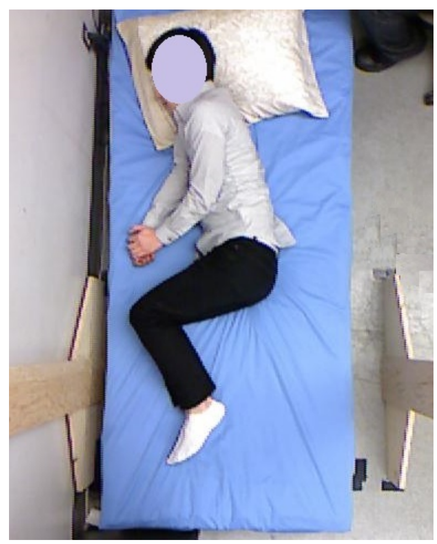

(b) Sample of overhead image

Figure 3.8: Video recording setup for ground truth labelling

The following experiments were tested against ground truth labelling. Figure 3.8 shows a video camera rigging for the ground truth visual image collection. All posture labels were marked manually from the visual images.

3.3.2 Sparse Classification Results

Table 4.1 summarizes the precision and recall results of 6 posture classification using the set of geometric features with different classifiers. The Sparse Classifiers with Maximum Sum of Class Coefficients (MSCC) heuristic and Minimum Class Residual (MCR) heuristics show a 20% improvement in accuracy over Decision Tree and Nearest Neighbor classifiers, and 6% improvement in accuracy over Nearest Subspace.

Table 3.4: Accuracy comparison to other classifiers

	Precision	Recall	f-measure*
C4.5 Decision Tree	57.0%	56.8%	56.9%
k-Nearest Neighbor	64.7%	62.1%	63.4%
Nearest Subspace	77.0%	76.5%	76.8%
Sparse Classifier (MC)	**65.4%**	**61.0%**	**63.1%**
Sparse Classifier (MSCC)	**83.1%**	**82.7%**	**82.9%**
Sparse Classifier (MCR)	**83.5%**	**82.9%**	**83.2%**

*f-measure is the harmonic mean of precision and recall

It is noted that the Maximum Coefficient (MC) heuristic does not show any improvement in the accuracy over Nearest Neighbor. The reason was given previously and is such that after the transformation into the sparse domain, the Maximum Coefficient (MC) is a metric similar in nature to Nearest Neighbor. It essentially finds the single training sample that maximizes its representativeness to the test sample, and does not take into account the class membership. Nearest Subspace does take into account class membership and hence exhibits a fair accuracy. The downside to Nearest Subspace is that it requires multiple optimization problems to be solved, i.e., one for each class. It is noted that the Sparse Classifiers only require a single run as it treats all the class samples as one sample space.

Table 3.5: Confusion Matrix Nearest Neighbor

	LL	LF	P	RL	RF	S	Recall
LL	123	6	7	26	41	83	43%
LF	3	194	14	39	3	33	68%
P	1	27	234	0	19	5	82%
RL	46	21	0	171	6	42	60%
RF	45	9	14	25	185	12	64%
S	42	6	3	20	5	210	73%
Precision	47%	74%	86%	61%	71%	55%	

Table 3.6: Confusion Matrix Nearest Subspace

	LL	LF	P	RL	RF	S	Recall
LL	143	0	2	51	41	20	66%
LF	3	243	21	30	4	6	79%
P	10	16	253	0	20	4	83%
RL	27	17	0	183	2	9	76%
RF	44	7	10	13	262	5	77%
S	59	3	0	9	1	242	77%
Precision	50%	85%	88%	62%	90%	84%	

To look more closely at the results of the Spare Classifiers, the confusion matrices are given in Tables 3.5 to 3.9. Table 3.5 shows the confusion matrix for Nearest Neighbor classifier and one notes the similarity with the Maximum Coefficient Sparse Classifier (MC) in Table 3.7.

Generally, the log postures are harder to recognize than the other postures. Recall for both Left Log and Right Log are always lower than the other 4 postures,

Table 3.7: Confusion Matrix Sparse Classifier (MC)

	LL	LF	P	RL	RF	S	Recall
LL	149	29	24	19	23	42	52%
LF	15	168	26	30	18	29	59%
P	9	24	202	6	20	25	71%
RL	40	25	5	176	22	18	61%
RF	11	22	23	19	194	21	67%
S	44	13	11	9	11	198	69%
Precision	56%	60%	69%	68%	67%	59%	

Table 3.8: Confusion Matrix Sparse Classifier (MSCC)

	LL	LF	P	RL	RF	S	Recall
LL	207	6	2	15	6	50	72%
LF	4	249	14	6	9	4	87%
P	1	22	245	1	12	5	86%
RL	14	27	1	219	12	13	77%
RF	0	9	14	3	262	2	90%
S	30	6	2	1	3	244	85%
Precision	81%	78%	88%	89%	86%	77%	

while the precision rates are generally lower but not always. The log postures are most similar to each other as both have legs outstretched and arm positions can vary. The next most similar posture is Supine. This is seen in all of the confusion matrices as high counts for predicted switched Left Log and Right Log, and Supine.

Figure 3.9 shows two examples of misclassifications of hard log postures. The left image shows Left Log posture that is incorrectly identified as Right-Log. This typical kind of error can be explained from the pressure map that is extended behind the subject's back. Hence misclassifications can occur as the pressure

Table 3.9: Confusion Matrix Sparse Classifier (MCR)

	LL	LF	P	RL	RF	S	Recall
LL	202	8	5	18	5	48	71%
LF	2	252	18	5	6	3	88%
P	1	22	249	1	10	3	87%
RL	12	28	2	225	10	9	79%
RF	0	11	15	5	257	2	89%
S	27	9	3	1	3	243	85%
Precision	82%	76%	85%	88%	88%	79%	

image now looks like a Right Log image. Similarly, the right image shows Right Log posture that is incorrectly identified this time as Supine. Visually, this image is hard to not identify as Supine.

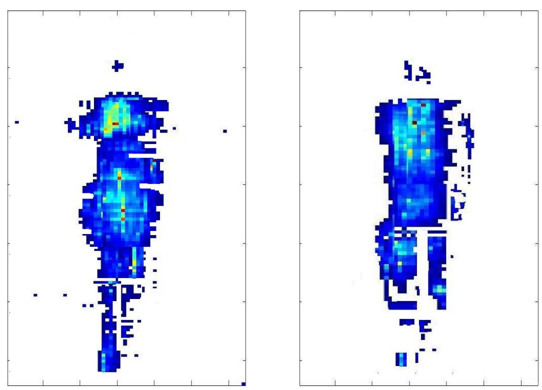

(a) Left Log posture misclassified as Right Log

(b) Right Log posture misclassified as Supine

Figure 3.9: Misclassified Postures

3.3.3 Overnight Continuous Monitoring

To further evaluate the accuracy of the pressure sensitive bedsheet system, posture analysis for continuous overnight monitoring is tested. In this study, 3 patients are monitored over 3 nights on the bedsheet. Overhead video images of the subjects were recorded to manually extract the ground truth postures. Roughly 2600 pressure images were recorded for each overnight session lasting 7-9 hours. As subjects do not move much while sleeping, the sampling rate was decreased to 10s per sample for the sake of memory constraints in the tablet.

The results using the HMM framework with subject dependent testing are analyzed. With three complete overnight data for each subject, two of the sets are used for subject training and the third is used for testing. This is repeated with cross validation. The results shown in Table 3.10 compare two classification schemes: one with Hidden Markov Models and the other with plurality voting over sliding window of size 10. Both of these classification methods showed small improvements in the accuracy of posture analysis over long durations and sequential pressure imaging, compared to static posture analysis in the previous sections.

Table 3.10: Experimental results for overnight studies

	Precision	Recall	f-measure
HMM with MC	78.4%	73.6%	75.9%
HMM with MSCC	86.5%	84.7%	85.6%
HMM with MCR	86.0%	84.4%	85.2%
Sliding Window Plurality with MC	73.9%	76.5%	75.2%
Sliding Window Plurality with MSCC	83.7%	84.5%	84.1%
Sliding Window Plurality with MCR	83.8%	84.8%	84.3%

For sliding window plurality voting, the predicted posture is chosen as the posture with the relative majority compared to the other postures, and is updated with a sliding window of fixed size over the set of consecutive previous images. In each group of consecutive samples, the simple plurality vote of the predicted test sample classifications is taken as the classification for that grouping of image samples, i.e., the posture that is predicted most frequently.

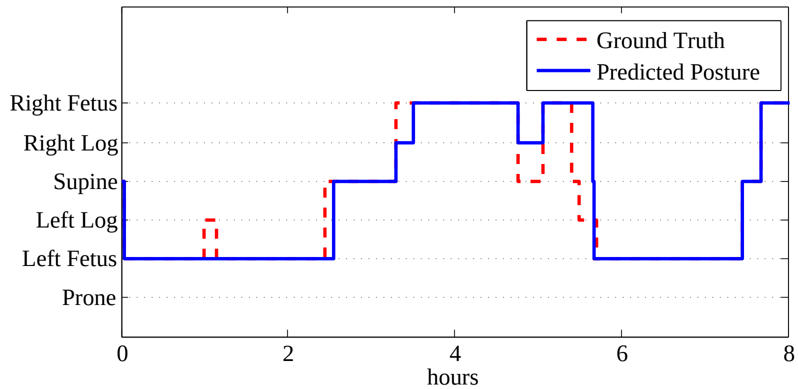

Figure 3.10: An example of one subject's 8 hour continuous monitoring study

Overall, the results of continuous monitoring study show that classification accuracy can be improved when sequential static images are available. The HMM based sequential methods show roughly 2-3% improvement over static image classification for the Maximum Sum of Class Coefficients (MSCC) and Minimum Class Residual (MCR) heuristics. Interestingly, the HMM with Maximum Coefficient method shows the largest improvement. This may be explained by the fact that Nearest Neighbor type methods benefit most by the clustering of points as more data is considered. A sliding window size of 10 improves the classification by a percentage point over static image classification, however this may not be statistically significant over a small total sample size.

Figure 3.10 shows the result of one of the test subjects for an 8 hour overnight continuous monitoring session with predicted and true postures given. The subject is a typical sample of the progression of posture sequences. Here the subject had 12 discernible posture changes.

3.3.4 Stability Analysis

This section analyzes the robustness of the classification by firstly investigating the variation during cross validation. The question of whether patient height affects classification results is also investigated. Stability is a measure that describes how closely the classifier evaluates results if given different data. For this work, stability is calculated by finding the variation in accuracy over a number of runs. Figure 3.11 shows the classification variation for the 6 postures for each of the classifiers.

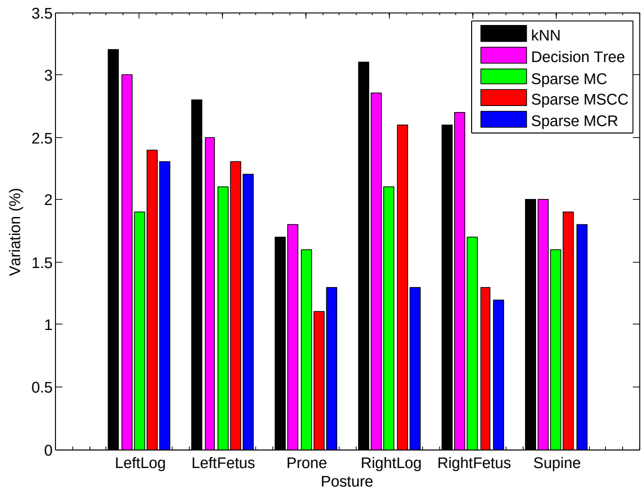

Figure 3.11: Classification variation for 6 postures

The Sparse Classifiers have smaller variation values than the other traditional classifiers. This indicates that sparse classification is a more stable classification method. The log postures have a higher variation in classification accuracy than the other postures. This is explained by the higher variation in weight distribution for these postures. In the data, the log postures vary much between fully lying on the side and lying on the back.

Although the Maximum Coefficient (MC) Sparse Classifier achieves the same accuracy as Nearest Neighbor, it does perform better when considering its enhanced stability.

The robustness of the algorithm with regards to input errors, such as from disconnected wires in the bedsheet, is also considered. The effect of this would be missing rows or columns of data in the pressure image. Figure 3.12 shows experi-

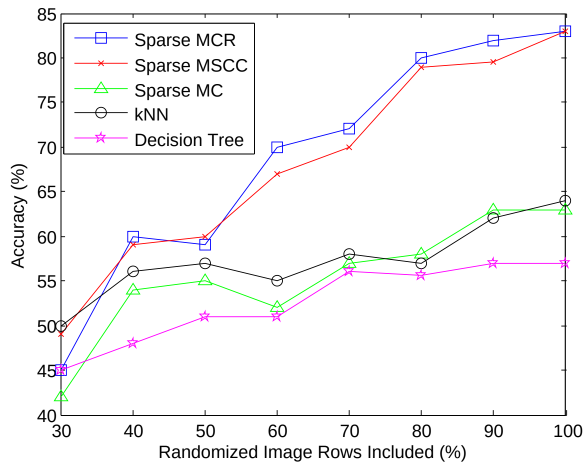

Figure 3.12: Classification robustness with random row deletions

mentally how a random number of failures of bus lines will affect the accuracy of the classification result. Roughly 20% of the hardware connections can fail with only a 4% drop in classification accuracy.

Figure 3.11 shows results for a subset of patients based on subject height. The tested groups were subjects with height below 165cm (approximately 1/3 of the total patients), subjects with height above 178cm (approximately 1/3 of the total patients), and the remaining subjects. It is interesting to note that, using the Sparse Classifier, the taller subset of patients did exhibit a higher classification accuracy compared to the mean accuracy, while the shorter subjects showed a lower classification accuracy. This is not true for the Nearest Neighbor classifier. The fact that the Nearest Neighbor classifier does not work well for the extremes of patients heights can be explained by the nature of the classifier in that there are no near neighbors. It can be postulated that the reason the Sparse Classifier works better for taller subjects is due to the restriction in bed size. Taller people may not have as much room to move as shorter people and so they have less variation in sleep posture.

Table 3.11: Accuracy (f-measure) of subjects S grouped by height

	S $\leq$ 165cm	165cm < S <178cm	S $\geq$ 178cm
k-Nearest Neighbor	61.1%	67.3%	60.0%
Nearest Subspace	75.5%	77.1%	76.0%
Sparse Classifier (MC)	61.1%	66.1%	62.1%
Sparse Classifier (MSCC)	80.6%	83.0%	85.6%
Sparse Classifier (MCR)	81.1%	83.1%	85.4%

3.3.5 Feature Selection

In this section, the effect of feature selection in classification is examined. 32 features are extracted from the pressure image set for classification. It is most certainly the case that some features are redundant or do not have any effect on classification results. Sequential Forward Selection (SFS) is employed to find subsets of features that are most descriptive of the whole feature set [JKP94]. This method is considered a wrapper method, i.e., the feature selection is based on using the classification results themselves and the selection process wraps around the classification.

With this method, the first feature is selected by testing each feature individually in classification. The feature with the highest accuracy performance is chosen first. In the second round of selection, each of the remaining features is used with the first feature in classification. The feature resulting in the highest accuracy is chosen as the second feature in the feature selected subset. This process continues as one feature is added at a time until all of the features are selected. Since the classification always uses previously selected features, redundant features are not selected until the end.

Figure 3.13 shows the relationship between number of selected features chosen using SFS and classification accuracy for each of the classifiers. Accuracy generally

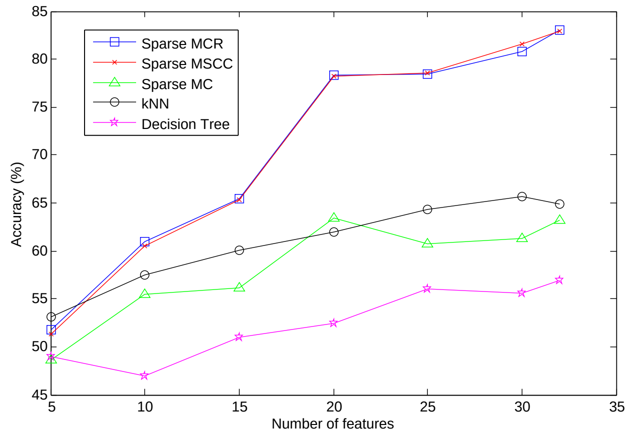

Figure 3.13: The impact of feature dimension on classification accuracy based on Sequential Feature Selection

increases as more features are used for all of the classifiers. There is a sharp increase in accuracy using the Sparse Classifier with both Maximum Sum of Class Coefficients (MSCC) and Minimum Class Residual (MCR) heuristics, from 65% to 78% between 15 features and 20 features. Moreover the three Sparse Classifiers appear to have a threshold at 20 features in the accuracy results, with a smaller rate of increase in accuracy as more features are used. The traditional kNN and Decision Tree show modest increase of about 10% throughout the whole feature selection process.

An alternative method of selecting features is based on filtering. Each of the features are evaluated based on how well they separate the data into the correct classes. Table 3.12 shows the order of features ranked by an information gain metric [CT91]. Information gain describes the reduction in information entropy caused by knowing the value of a feature. Features with high information gain allow better classification. Information gain, IG, is given by

$$IG(A,F) = Entropy(A) - \sum_{f \in F} \frac{|A_f|}{|A|} Entropy(A_f)$$

where A_f is the subset of dataset A for which feature F has value f. Entropy is

Table 3.12: Alternative method of ranking features by Single Feature Selection

InfoGain	Feat #	Feature	InfoGain	Feat #	Feature
0.887577	17	HipPoint(y)	0.262988	11	Reg7
0.616256	18	HipBox(x)	0.256317	5	Reg1
0.581828	20	HipBox(w)	0.252169	24	ShPoint(x)
0.554651	16	HipPoint(x)	0.234055	32	HipShDist
0.536393	14	Balance	0.215533	23	HipPtoBox
0.497846	19	HipBox(y)	0.200476	29	ShBox(h)
0.47028	22	HipArea	0.196697	3	Per50
0.443133	6	Reg2	0.186926	4	Per75
0.435716	13	Symmetry	0.186884	28	ShBox(w)
0.400952	10	Reg6	0.171033	2	Per25
0.359848	1	Coverage	0.168928	26	ShBox(x)
0.340698	21	HipBox(h)	0.153444	15	DirCurve
0.321448	25	ShPoint(y)	0.143608	30	ShArea
0.318234	9	Reg5	0.126994	12	Reg8
0.302024	27	ShBox(y)	0.12267	8	Reg4
0.277772	31	ShPtoBox	0.117452	7	Reg3

given by

$$Entropy(X) = -\sum_{i=1}^{n} p(x_i) log_2 p(x_i)$$

where $p(x_i)$ is the probability of sample x_i occurring in the dataset X. The features are chosen one at a time and the classification does not include previously selected features. The disadvantage of this method is that it does not take into account the redundancy in some of the features. In experiments, this method was shown not to be as accurate as the Forward Selection.

It is interesting to note, however, that the highest ranked features are those associated with hip location and bounding box. This can be expected since the different postures do vary much in the pressure points of the hip region. It is a strong indicator of side postures versus the supine and prone postures.

3.4 Conclusion

This work presents a sleep analysis design that monitors sleep posture using a pressure sensitive bedsheet. An application for such a system is to enable caregivers the ability to automatically identify when patients are at risk of developing pressure ulcers or when subjects experience sleep apnea. This work also presents the novel use of relevant features that can be extracted from pressure images, as well as state of the art classification methods. Three heuristics are developed for sparse classification, and experiments show that both Maximum Sum of Class Coefficients (MSCC) and Minimum Class Residual (MCR) heuristics produce reliable sleep posture estimation. Through experiments of individual images as well as continuous overnight sequences, the effectiveness of this method for sleep posture recognition is evaluated.

Pressure monitoring systems need not be limited to sleep posture recognition. In nursing home settings, evaluation of fall risk is a desirable endeavor. Advanced beds are now being developed that can re-distribute support to different regions of the bed [Hil] and also aid in the heat flow through the bed mattress. Using pressure point monitoring, the goal is to increase healing speed of patients.

Future work also involves the ability to monitor transitional states as patients move between pre-defined stable classified postures. There are more challenges here because of the large variations in different subjects' motions. 3D model reconstruction of patients from 2D pressure image is another goal that can be accomplished using the results of this research work.

CHAPTER 4

Fine Grained Bodyparts Localization

4.1 Background

With recent advances in technology, pressure sensors are being increasingly deployed in various devices for measuring pressure on the body. Current commercial systems in the form of sheets are undergoing greater use [Xse, Vis]. These sensors have a variety of resolutions and are able to accurately measure pressure distributions under the body. Other research projects are more focused on developing low-cost disposable sheets compared to existing commercial systems. A capacitive pressure sensor array was designed by Yip et al. with an estimated low cost of $\$50/\mathrm{m}^2$ [YHW09]. Research by Lee and Butler included blood oxygenation sensors alongside pressure sensor to analyze the development of pressure ulcers [LB13].

Using a commerical pressure sensitive mat, Farshbaf et al. located bodyparts with a reported average accuracy of 85.7% [FYB13]. Their method involved extracting the body boundary through filtering, dilation, and edge detection. Then, with Constrained Delaunay Triangulation, they were able to prune a skeletal graph. Finally, by applying Dynamic Time Warping to the skeleton, the nodes and leaves can be matched to a pre-defined bodypart template of the human body. In conjunction with Siemens magnetic resonance imaging (MRI), Grimm et al. used constrained articulated ellipsoid modelling of the body to minimize the error between the pressure image and generated images [GSH11]. In this case, bodypart localization helped to fine tune specific scans of the patient. To date, these works are the only published prior art in bodypart localization using pressure sensors with the purpose of pressure ulcer prevention.

Figure 4.1: The pressure sensitive bedsheet setup with sensing eTextile layers.

The focus of this work is localizing bodyparts within pressure images, employing a dense pressure sensitive textile bedsheet and applying pressure image analysis for bodypart localization. In contrast to the previously mentioned work that reduced a pressure image of the body to a skeletonized frame, this method uses a Pictorial Structure model of the body [FE73] and calculates the best locations based on both the appearance and the spatial information of the pressure image. Due to coupling effects in the sensor array, i.e., neighboring sensor leakage, boundary detection and skeletonization does not always work as there are regions that do not have much pressure, such as behind the knees when a patient is lying supine (on the back). This method instead uses a simple model matching metric and deformation costs in a minimally pre-processed image. It is also due to coupling effects of sensor arrays that constrained articulated models can also fail. By using deformation costs, Pictorial Structures account for variations in the pressure around high pressure regions. Furthermore, constrained articulated models assume fixed size of torso and limbs, which cannot account for variations in patient height and weight.

With the end goal of monitoring pressure ulcer occurrence, the locations of bodyparts can be found and this information can be fed into patient monitoring systems that track the accumulation of pressure and generate alerts using efficient turning schedules [OYF11], or risk maps [MMR11]. The work presented in this work targets the accurate localization of bodyparts followed by its application in respiratory rate monitoring.

4.2 Method

This method is based on the pictorial structures model, proposed by Fischler and Elschlager [FE73], for identifying structured objects in images. Felzenszwalb and Huttenlocher improved the matching efficiency of the parts based algorithm using distance transforms within dynamic programming [FH05]. The original formulation of finding bodyparts is described here.

Each part of the human body can be represented as a vertex in a tree. For instance, the head, shoulders, hands and feet are nodes in a graph connected by edges. Given an image I, a mismatch cost $m_j(I, l_j)$ is defined as a measure of how much the image I matches a bodypart j at the location $l_j = (x_j, y_j, \theta_j)$ where x_j, y_j are the co-ordinates of the center of the bodypart model with rotation angle θ_j. A low value of mismatch means the bodypart is well recognized at that location.

In addition to the cost for how well the appearance of each bodypart matches its template, there is a cost for the relationship between bodypart locations. For bodyparts i and j, a deformation cost $d_{ij}(l_i, l_j)$ gives a measure of how far the bodyparts deviate from their expected respective locations. For instance, the hip and shoulders are known to be separated by the spine length. So for a given set of bodypart templates and connections between them, the best configuration of bodyparts $L = (l_1, ..., l_n)$ in an image minimizes the total cost of mismatch for all parts and deformation between all pairs of parts:

$$\arg\min_{L}\left(\sum_{allparts} m_j(I,l_j) + \sum_{allpairs} d_{ij}(l_i,l_j)\right). \tag{4.1}$$

This formulation takes exponential time in the number of bodyparts n, however with the tree representation of bodyparts, this can be solved more efficiently as a chain of computations using dynamic programming as follows. For any leaf vertex (i.e., has no children), its best location $\hat{l}_j$ can be calculated as a function of its parent location l_i. So the best leaf vertex location is a function of parent location:

$$B_j(l_i) = \arg\min_{l_j}\left(m_j(I,l_j) + d_{ij}(l_i,l_j)\right). \tag{4.2}$$

For a non-leaf, non-root vertex, its best location $\hat{l}_j$ as a function of its parent location l_i is given by

$$B_j(l_i) = \arg\min_{l_j}\left(m_j(I,l_j) + d_{ij}(l_i,l_j) + \sum_{Ch(j)} B_c(l_j)\right), \tag{4.3}$$

where $Ch(j)$ means children vertices of j and $B_c(l_j)$ are the costs of the best locations of the children of j. This is already calculated and memoized via the dynamic programming methodology.

Then for the root vertex (no parent), its best location is

$$\hat{l}_j = \arg\min_{l_j}\left(m_j(I,l_j) + \sum_{Ch(j)} B_c(l_j)\right), \tag{4.4}$$

where $B_c(l_j)$ is known for each of the children of j. This formulation (Equations 4.2 to 4.4) reduces the number of computations from exponential to polynomial while still producing the globally optimal solution.

To compute the mismatch cost $m_j(I,l_j)$ for each bodypart, one selects a representative template and, in this work, the bodyparts are simply represented as rectangular boxes surrounded by a border due to ease of calculation (Figure 4.2).

The size of template is proportional to the height of the subject. To account for different pressure images due to varying weights of the subjects, the image I is binarized at different thresholds. A convolution operation of this kernel with the binary images efficiently gives the mismatch cost at all locations. This computes how many pixels do not match inside the inner box and within the border. Then, mismatch cost is the smallest cost across all threshold levels for each location.

-1	-1	-1	-1	-1	-1	-1	-1	-1	-1	-1	-1	-1	-1	-1	-1	-1	-1
-1	-1	-1	-1	-1	-1	-1	-1	-1	-1	-1	-1	-1	-1	-1	-1	-1	-1
-1	-1	1	1	1	1	1	1	1	1	1	1	1	1	1	1	-1	-1
-1	-1	1	1	1	1	1	1	1	1	1	1	1	1	1	1	-1	-1
-1	-1	1	1	1	1	1	1	1	1	1	1	1	1	1	1	-1	-1
-1	-1	1	1	1	1	1	1	1	1	1	1	1	1	1	1	-1	-1
-1	-1	1	1	1	1	1	1	1	1	1	1	1	1	1	1	-1	-1
-1	-1	1	1	1	1	1	1	1	1	1	1	1	1	1	1	-1	-1
-1	-1	1	1	1	1	1	1	1	1	1	1	1	1	1	1	-1	-1
-1	-1	1	1	1	1	1	1	1	1	1	1	1	1	1	1	-1	-1
-1	-1	1	1	1	1	1	1	1	1	1	1	1	1	1	1	-1	-1
-1	-1	-1	-1	-1	-1	-1	-1	-1	-1	-1	-1	-1	-1	-1	-1	-1	-1
-1	-1	-1	-1	-1	-1	-1	-1	-1	-1	-1	-1	-1	-1	-1	-1	-1	-1

Figure 4.2: Template for bodypart mismatch cost. The mismatch cost of the bodypart model is the sum of mismatched pixels within the inner rectangle and matching pixels in the border region.

To compute the deformation cost $d_{ij}(l_i, l_j)$ between bodyparts, this cost is defined to have the form

$$d_{ij}(l_i, l_j) = ||T_{ij}(l_i) - T_{ji}(l_j)||. \tag{4.5}$$

This is a simple distance metric between locations transformed to a common space. The transforms can be translations, rotations, and scaling, hence they are invertible (See Fig. 4.3). The effect of the transforms is to specify the expected relations between the locations, i.e., if two bodyparts have no deformation cost and are correctly positioned, then the transformed locations will coincide. The pairwise distance metric takes quadratic time in the number of locations. For every location of the parent, compute the distance to each location of the child. On the surface, quadratic time may seem satisfactory but this can be improved to linear time through the use of distance transforms [Bor86]. In fact, every pairwise distance between l_i and l_j need not be computed. From Equation 4.2, only the smallest sum of deformation cost and mismatch cost is needed at each location of l_i.

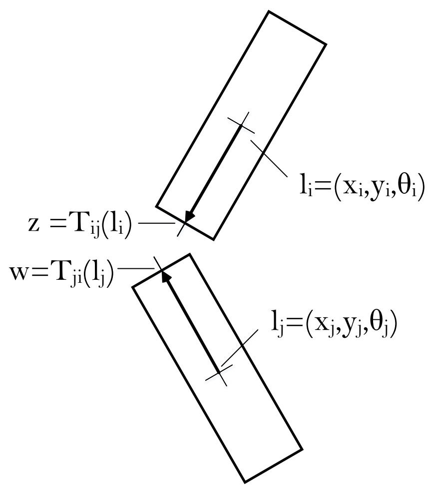

Figure 4.3: Example transformation of bodypart models

The generalized form of a distance transform given a function f is

$$D(z) = \min_w \left(||z - w|| + f(w) \right), \tag{4.6}$$

where z and w are locations in a grid. This formulation states that, for every location z, it finds the closest location w with the smallest value for $f(w)$.

In Equation 4.6, z maps to a translated location for l_i, i.e., $z = T_{ij}(l_i)$. w maps to a translated location for l_j, i.e. $w = T_{ji}(l_j)$. $f(w)$ is a function that maps to $f(w) = m_j(I, T_{ji}^{-1}(l_j))$. So now Equations 4.2 and 4.3 become

$$B_j(l_i) = D(T_{ij}(l_i)). \tag{4.7}$$

With these equivalences, Equation 4.2 is expressed in a form where the generalized distance transform applies.

$$B_j(l_i) = D(T_{ij}(l_i)) = \min_{l_j}\Bigg(||T_{ij}(l_i) - T_{ji}(l_j)|| \\ + m_j(I, T_{ji}^{-1}(T_{ij}(l_i)))\Bigg). \tag{4.8}$$

For nodes that are not leaves or root, Equation 4.3 converts to

$$B_j(l_i) = D(T_{ij}(l_i)) = \min_{l_j}\Bigg(||T_{ij}(l_i) - T_{ji}(l_j)|| \\ + m_j(I, T_{ji}^{-1}(T_{ij}(l_i))) \\ + \sum_{Ch(j)} B_c(T_{ji}^{-1}(T_{ij}(l_i)))\Bigg). \tag{4.9}$$

Now the final discussion describes how to speed up the calculation of Equation 4.7. For the leaf nodes, an array $D[x, y, \theta]$ is initialized with the values of $m_j(I, T_{ji}^{-1}(T_{ji}(l_j)))$, which is just the mismatch cost of the child but translated to a new location in the same space as the parent. For non-leaf nodes, the array $D[x, y, \theta]$ initializes with the values of

$$m_j(I, T_{ji}^{-1}(T_{ij}(l_i))) + \sum_{Ch(j)} B_c(T_{ji}^{-1}(T_{ij}(l_i))), \tag{4.10}$$

which is the mismatch cost of the child (translated to a new location in the same space as the parent) plus the cost of the children. The values of $D[x, y, \theta]$ can be updated according to

$$D[x, y, \theta] = \min(D[x, y, \theta], \\ D[x-1, y, \theta] + k_x, \\ D[x, y-1, \theta] + k_y, \\ D[x, y, \theta-1] + k_\theta), \tag{4.11}$$

where k_x, k_y, k_θ are constants that account for different pixel scales. This is executed in sequence starting from array point [1,1,1] linearly through the array which is followed by a second sweep in the reverse direction.

$$
\begin{aligned}
D[x, y, \theta] = \min(D[x, y, \theta], \\
& D[x+1, y, \theta] + k_x, \\
& D[x, y+1, \theta] + k_y, \\
& D[x, y, \theta+1] + k_\theta), \qquad (4.12)
\end{aligned}
$$

With this computation, the best location of the child is found for all locations of parents. Continuing this pattern for all vertices, the best location of the root can be solved efficiently, and the best location of the children are traced from the parents.

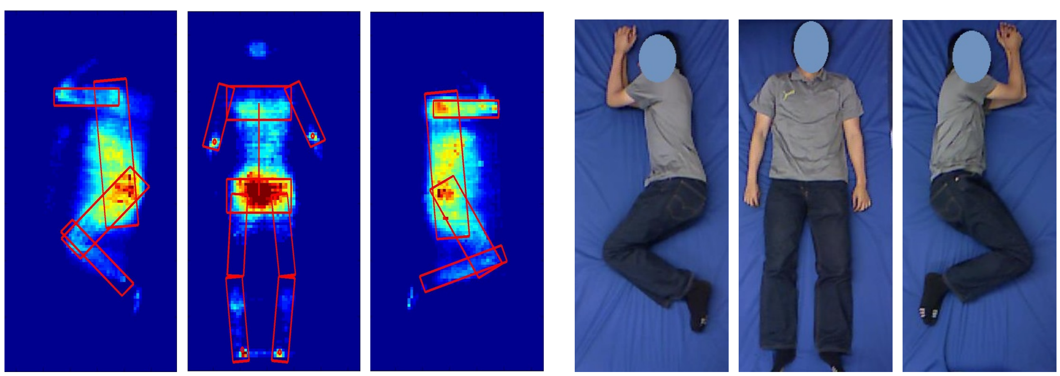

Figure 4.4: Sample image results for bodypart localization in the right lateral, supine, and left lateral postures.

4.3 Experimental Results

4.3.1 Experimental Setup

A pilot study to evaluate the performance of the system for localization of body-parts is run. There are 12 subjects in the experiment with 9 male and 3 female subjects. The weights of the subjects range from 50kg to 85kg, and height between 155cm and 188cm. For the sake of consistency, the bedsheet system is also deployed on a standard twin-size coil spring mattress during the experiments.

Figure 4.5: Setup for ground truth recording

In the data collection, 40 samples were recorded for each of the 3 postures (supine, left and right) for each subject. At fixed intervals, the pressure image of the subject's posture was recorded while the subject maintained a comfortable sleeping position. Variations in body, arm and leg positions were allowed and the system is tested on a range of positions that fall within the 3 defined postures. The following experiments were tested against hand labelled ground truth from direct overhead camera recordings.

Fig. 4.5 shows a video camera rigging for the ground truth visual image collection using a Microsoft Kinect sensor. The bodyparts in all of recorded images were hand labelled.

4.3.2 Experimental Results

Once each of the bodypart models is located, fine tuning of the locations of the high pressure points proceeds by finding the center of mass within the bodypart

Table 4.1: Accuracy of bodypart localization

Posture	Bodypart	Accuracy Farshbaf [FYB13]	Error Grimm [GSH11]	Accuracy† (%)	Error‡ (inch)
Supine	Shoulder	93.3%	1.7” *	92.4%	1.2”
	Left Elbow	86.7%	-	87.1%	1.6”
	Right Elbow	80.0%	-	86.2%	1.7”
	Sacrum	93.3%	1.7”	94.7%	0.9”
	Left Heel	80.0%	-	93.1%	1.0”
	Right Heel	80.0%	-	93.7%	1.0”
Left	Shoulder	86.7%	2.9”	94.5%	0.9”
	Elbow	76.7%	-	82.1%	2.2”
	Hip	93.3%	2.0”	91.9%	1.3”
	Knee	-	3.3”	90.0%	1.8”
Right	Shoulder	90.0%	2.3”	92.1%	1.2”
	Elbow	96.7%	-	84.5%	2.0”
	Hip	90.0%	2.0”	92.2%	1.2”
	Knee	-	3.3”	85.2%	2.0”
Average		85.7%	2.7”	**89.8%**	**1.4”**

†Accuracy is percentage of bodyparts within 1 inch of groundtruth.

‡Error is Euclidean distance from groundtruth location.

*Grimm et al. reported neck location instead.

model. For the heels and elbow, the center of mass is restricted to the lower half of the bodypart model.

Figure 4.4 shows a sample of bodypart localization results in right lateral, supine, and left lateral postures. Lateral postures are defined by 4 bodypart models and supine posture is defined by 8 bodyparts models. Table 4.1 summarizes the accuracy of bodypart localization for the 3 postures compared against prior work by Farshbaf et al. [FYB13] and Grimm et al. [GSH11]. The same metrics as described in the prior work are used here, where error is measured by Euclidean distance in inches between the tested and ground truth locations, and accuracy is calculated as the percentage of bodyparts that have error of less than 1 inch. In these experiments, the elbow resulted in the lowest localization accuracy. This can be explained by the relative weakness in pressure compared to the high pressure of the shoulder.

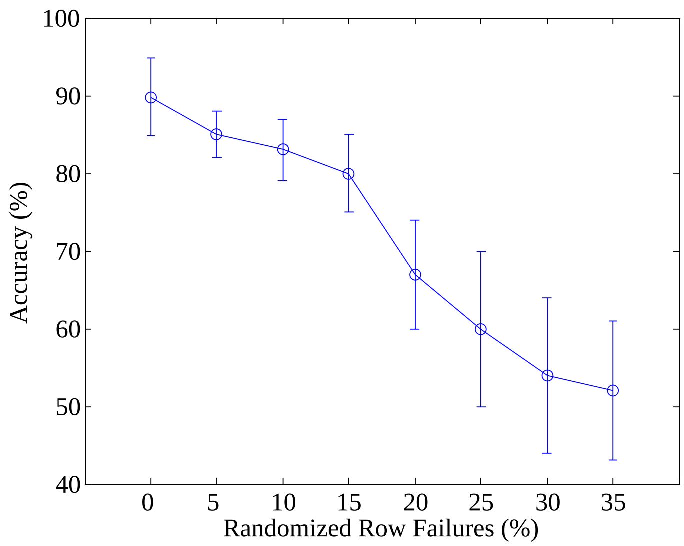

Figure 4.6: Accuracy of bodyparts localization with sensor input failures. Error bars indicate range of values for different subjects.

The robustness of this method is evaluated with random sensor failure. If a sensor input fails, the pressure image shows missing rows and columns, i.e., 64 pixels are eliminated for each row error and 128 pixels for each column error. Figure 4.6 shows experimentally how a random number of line failures in the pressure sensor hardware affect the average accuracy of the localization result. Overall, this method can tolerate 8% loss of accuracy while losing more than 15% of the data.

Table 4.2: Average Pressure at High Risk Regions for a Subject

Bodypart (posture)	average pressure* (x 10^{-3})
Sacrum (supine)	2.09 ± 0.13
Shoulder (lateral)	2.01 ± 0.13
Hip (lateral)	1.92 ± 0.11
Heel (supine)	1.52 ± 0.12
Elbow (supine)	1.43 ± 0.10
Shoulder (supine)	0.80 ± 0.09
Non risk areas	< 0.2

*Pressure values given are the pixel values when sum of pixels is normalized to 1.

Table 4.2 shows the average pressure of a sample subject. For this method of bodypart localization, the total accumulation of pressure can be recorded to facilitate pressure ulcer monitoring and prevention.

This work presents a method to localize bodyparts using a pressure sensitive bedsheet. The purpose of such a system is to enable caregivers the ability to automatically identify where patients are at risk of developing pressure ulcers. The experiments showed an overall localization accuracy of 89.8% for high risk regions such as the hip, heels, and shoulders.

4.4 Application of Bodypart Localization: Respiratory Rate Monitoring

This chapter has presented a method for bodypart localization from a pressure sensitive bedsheet. The remaining part of the chapter describes an application of this work, namely respiratory rate monitoring.

4.4.1 Background in Respiratory Rate Monitoring

There are three main categories of respiratory rate monitoring: on-body, indirect contact, and non-contact. On-body sensors are either directly attached on the skin or wearable through straps. The main concern with on-body sensors is their obtrusive nature and setup issues. Hospitals use pulse oximeters, such as the Nellcor Respiratory Monitor [Cov], to estimate respiratory rate from oximetry measurements on the patient's finger. However, the results are often inaccurate when patients have abnormal levels of oxygen saturation or low pulses [DeM07]. Respiratory Inductance Plesthysmography (RIP) is a dual belted sensor worn around the chest and abdomen. As patient's body expands and contracts during breathing, this sensor reflects changes in the inductance of its coils. Now, many sleep centers use this sensor solution, which is recommended by the American Academy of Sleep Medicine [Car08]. Another similar method is Impedance Plesthysmography, which also uses a belted sensor to measure physical expansion of the chest [KKW64]. Bates et al. placed 3-axis MEMS sensors on the patient's torso to continuously monitor respiratory rate from the acceleration and angle acceleration information[Bat10]. Outside of the hospital or sleep labs, commercial on-body sensor systems can be used. SecuraPatch [Sec], a small wireless adhesive sensor, can monitor respiratory rate and other vital signals during all day activities.

The second category of respiratory rate monitoring is indirect contact. Typically, this method involves sensors embedded in the mattress, sheet or pillow, which overcomes the discomfort issues inherent with on-body sensors. An air mattress sensor system [CHY05] allows measurement of the respiration and heart beat movements without use of any on-body sensor. However, the shape, type, or thickness of the mattress may introduce noise to the sensed data. In research conducted by Chen et al. [CZN05], a pressure sensor was put under the pillow to acquire pulsatile pressure signal. The respiration rhythm can be then inferred from the pressure signal. However, it required users to sleep in a restricted position. A hydraulic bed sensor [HS10] has been developed to non-invasively monitor pulse and respiration during sleep. Another type of indirect contact sensor is capacitance sensor which measures the changes in electrical permittivity above the sensor caused by air in the lungs [HTW10]. Again, it required the subject to be localized directly above the sensor. Using hetero-core fiber optic pressure sensors, Nishyama et al. [NMW11] relaxed the restriction of sleep pose a little further by having a wider sensitivity to small pressure changes and could account for large changes.

The third category of respiratory rate monitoring is non-contact. For instance, using video or other electromagnetic radiation sensing [XGL12]. Current developments in video analyses can measure respiratory rate and heart rate by analyzing the small changes in color of subjects' faces [PMP10]. The Philips Vital Signs Camera [Phi] application on iOS devices performs this contact-less measurement of breathing rate. However, using video cameras leads to a concern about patient privacy in hospital, and lighting during the night can be a significant problem. The use of infrared sensors can diminish some of these issues. Murthy et al. used an infrared imaging system to detect the temperature change of exhaled air out of patients' mouths [MPT04].

In summary, non-contact based respiratory rate monitoring has the advantage of non-invasiveness, however still needs to be localized, while contact sensors are obtrusive and need manual setup. On the other hand, this system, a high density pressure sensitive bed sheet, is non-invasive, comfortable and can measure respiration at any location on the mattress. It is able to provide sufficient accuracy to be used as a screening tool for changes in respiration.

4.4.2 Respiration Rate Monitoring with Bedsheet

In order to extract a better respiratory signal, chest location needs to be localized. This is because most of a human's body weight when lying is distributed in the torso area; thus, geometric features can easily capture static torso information even if the pressure among extremities varies or the subject body is relocated.

Once the torso is identified, the pressure values around the chest area can be extracted to increase the accuracy of breath detection and respiratory rate identification. After drifting compensation, four respiratory related features are analyzed in time series: the maximum pressure sensor value, sum of all pressure sensor values, standard deviation of all pressure sensor values, and the maximum singular value of the chest area. Respiratory signal can be observed directly by searching for peek values of these time-series feature curves.

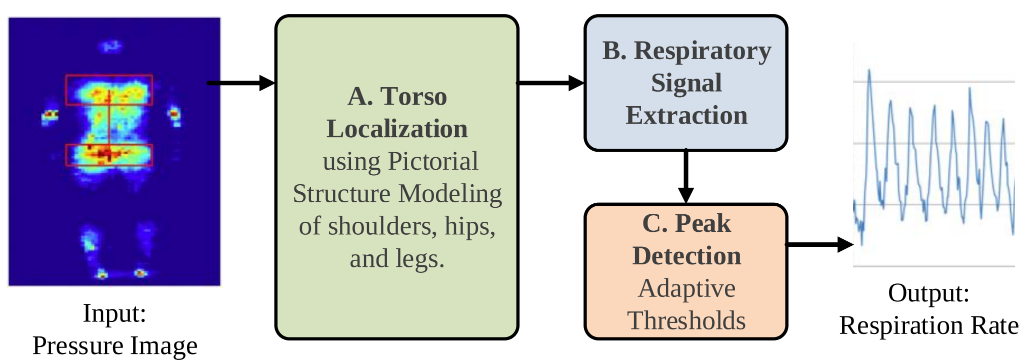

Figure 4.7: Respiration Monitoring Flow consists of three components: A. Torso Localization; B. Respiratory Signal Extraction; C. Peak Detection.

The method for monitoring respiration rate is composed of three parts: torso localization, respiratory signal extraction, and peak detection (see Figure 4.7). Locating the torso area in the time-indexed pressure images reduces interference caused by extremity movement. The torso localization algorithm is what was described previously for bodypart localization. Once the torso area is localized, the pressure values in the area of chest and stomach are used to extract respiratory signals using a vertical weighting calculation. A peak detection algorithm with adaptive thresholding is applied to mark breathing events and intervals. Fig. 4.7 shows the overview of the algorithm.

4.4.2.1 Respiratory Signal Extraction

This subsection describes the respiratory signal extraction method from the time series pressure regions. This results in a pressure indicator that is based on an observation that, while breathing, the pressure distribution along with vertical direction (from chest to stomach direction) varies with certain patterns and rhythms. For every frame, the pressure indicator sums the pressure values with their corresponding vertical directional coordinates:

$$Resp(t) = \sum_{(x,y) \in torso} \sum y * I[x, y](t). \tag{4.13}$$

The range of the pixels in the torso is the region between chest and hip bounding boxes which is enclosed by the bottom of the shoulder bounding box and the top of the hip bounding box. The calculated pressure indictor forms a time-series respiratory signal stream.

4.4.2.2 Peak Detection with Adaptive Thresholding

In general, a simple peak detection algorithm [Bil] is sufficient to recognize the periodic peak and valley of the time series data. However, arbitrary thresholding does not always work since the magnitude difference between peak and valley of time series data varies among testing subjects. Subjects breathing with moderate muscle activity in their shoulder or back area tend to generate large magnitude differences in the calculated pressure indictor time series. To accommodate the differences among subjects, the selected peak detection algorithm is augmented with adaptive threshold version as shown in the Algorithm 1.

Algorithm 1 Peak Detection with Adaptive Thresholds

Input: time series $data$ of size n

Output: number of detected breaths

Initialize: $lookformax$=true

$maxdiff$ = maximum magnitude difference in $data$
for $thresh = 0$ to $maxdiff$ **do**
    for all n points in $data$ **do**
        if $lookformax = true$ and $data.value < currentmax - thresh$ **then**
            Peak detected and set $lookformax$ = false
        else
            Update $currentmax$
        end if
        if $lookformax = false$ and $data.value > currentmin + thresh$ **then**
            Valley detected and set $lookformax$ = true
        else
            Update $currentmin$
        end if
    end for
    Record the number of breaths (peak and valley pairs) and the corresponding $thresh$ in graph
end for
Find the first flat region in graph and output the number of detected breaths

Given time series data of the extracted respiration signal, this adaptive threshold method profiles the relationship between the number of breaths and threshold values. A threshold is defined as the value difference by which a peak is recognized from surrounding data. So for each threshold value between 0 and the maximum magnitude difference in the data, the algorithm detects a peak when the data falls below the peak value by more than the threshold value. Similarly, a valley is detected when the data rises above the valley value by more than the threshold. Once all thresholds have been tested, it then finds the range of thresholds that have the least effect on the number of breathing events. This coincides with the flat area (see Fig. 4.8). It means that, within certain threshold ranges, the number of breathing events is consistent and implies those thresholds are less sensitive to the random hardware noise. The number of breathing events is recorded and the corresponding event intervals are used to calculate respiratory rate. A period of peak and valley is viewed as a complete respiration and the intervals between two peaks are viewed as breath intervals.

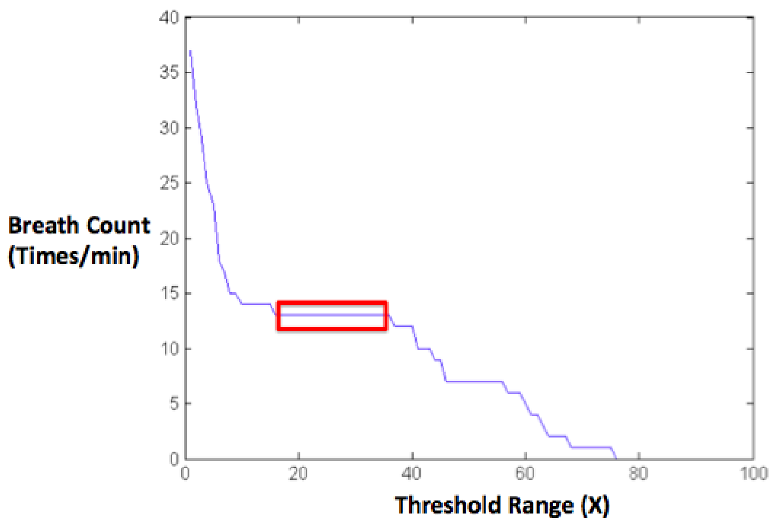

Figure 4.8: Number of Detected Breaths for Threshold Values

4.4.3 Experiments

12 subjects participated in the study with heights 152 to 190 cm, weights 46 to 83 kg. The high density pressure sensor sheet was deployed on top of a foam mattress with memory in a lab environment. The experimental goals were to evaluate the effectiveness of the torso localization algorithm for respiratory signals extraction on a regular soft bed environment. During experiments, subjects were allowed to

lie in their preferred posture and keep their regular lying habits. In addition, data was recorded in full without segmentation and truncation due to interferences caused by extremity movements. Full experiment processes were taped, breath events were timed and labelled manually from the taped videos according to the visible chest wall movement. Recording started when the subjects lied on top of the pressure sensing system in their preferred lying posture. They were asked to breathe as usual and not to make any large posture changes, such as rolling or sliding, during the recording. Furthermore, tilted bed situations as commonly seen in clinics were simulated by changing the tilt angles of the bed head and foot areas. For these tilted bed situations, the subjects were evaluated in supine posture only.

4.4.3.1 Results for Respiration Monitoring

Pressure values variation within the torso region is of most interest for respiratory signal extraction. In this experiment, respiratory signals were extracted from pressure image sequences when participants lied in common lying postures: supine, side, and prone for 10 minutes each. The method of torso localization was applied to the pressure image sequences to keep track of the regions between chest and stomach areas. Then signal extraction via vertical weighting calculation and peak detection methods were used to extract the breathing events. Table 4.3 summarizes the results and shows comparisons between the detected respiration events and the ground truth visually recognized from video recordings for all three lying postures. On average, the detected respiration events match well with ground truth across the three common lying postures. Different lying postures and extremities movements did not affect the quality of torso localization and the extracted respiratory signals.

Table 4.3: Results for respiration in three common lying postures (detected breaths / ground truth) over 10 minute periods.

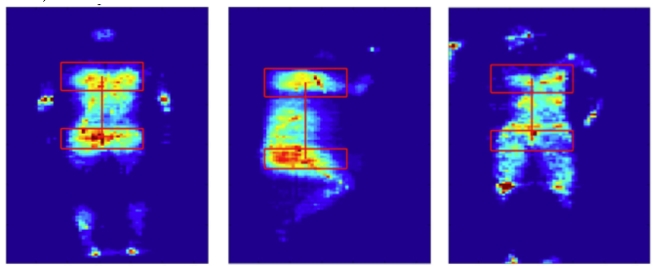

ID	Supine	Lateral	Prone
1	174/176	169/172	176/177
2	147/155	137/154	143/152
3	171/175	162/173	170/175
4	184/185	184/186	187/188
5	127/130	125/133	130/127
6	136/142	138/144	139/144
7	155/162	162/162	157/160
8	179/177	174/176	172/175
9	160/166	158/167	162/166
10	138/144	137/142	139/141
11	164/168	170/172	168/172
12	152/150	147/146	148/148
Avg.	**157.5/160.8**	**155.3/160.6**	**157.6/160.4**
Error	**2.0%**	**3.3%**	**1.8%**

4.4.3.2 Visualization of Respiration Motion

It is useful to illustrate the effect that vertical weighting calculation makes on respiratory signal extraction. There is an apparent geometrical delay from chest to stomach area and weighted pressure values with its vertical coordinates relative to the bounding box border emphasizes the respiration pattern. Visualizing the vertical momentum calculation can be a useful tool to investigate the nature of the geometrical delay phenomenon in pressure image sequences.

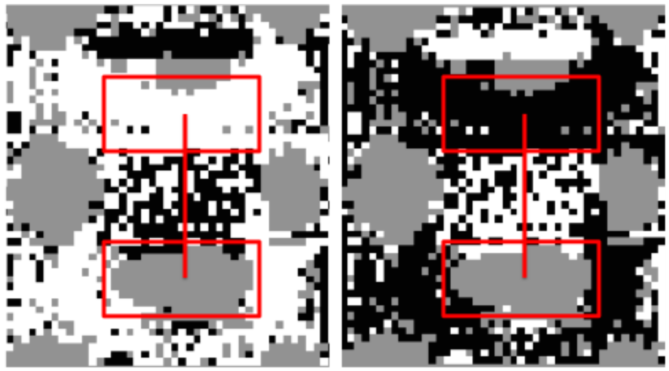

Figure 4.9: Examples of change in pressure distribution for inhaling and exhaling events. The red boxes show the location of detected shoulder and hip regions. The black and white areas show the locations of greatest pressure change.

In order to visualize calculated vertical momentum, results from peak detection algorithm are used. The peak detection algorithm returns a series of peaks and valleys from the pressure indicator time series. By subtracting two consecutive peak and valley indexed pressure images, the differences between images of peaks and valleys are obtained. Figure 4.9 visualizes the peaks and valleys of respiration by averaging the pressure differences between peaks and valleys. To better visualize the difference of chest and stomach area, all positive differences were marked as black and negative differences were marked as white. Gray area stands for no obvious pressure differences. It can be seen that pressure distribution of chest area is in opposite phase of the stomach area. This opposite phase phenomenon explains the reason why vertical weighting calculations can be a useful indicator for respiratory patterns extraction, because the geometrical delay from chest to stomach region is included in the indicator calculation.

4.4.3.3 Comparison of Body Region Locations

Three scenarios were evaluated and compared to demonstrate the importance of torso tracking: signals from the whole sheet without applying torso localization algorithm; signals from half of the sheet and centralized in the center of the weight; and signals from torso localized area, same as the results presented previously. The difference between the estimated breathing events and ground truth are reported in Table 4.4 for the supine posture.

Extracted respiratory events from torso localized areas showed good consistency with the ground truth. This is because during breathing, large periodic pressure variances are expected in the chest to stomach regions. Pressure variance outsides the torso regions can be viewed as interference which directly impacts the calculation of vertical weighted signal extraction. Interference caused by the extremities movements were time-varied and subject-dependent; therefore, the accuracy of respiratory signal extraction from the whole sheet largely was highly impacted by the movements of the participants. For the case of extracting signals from the area nearby the center of mass, the accuracy of respiratory signal extraction was reduced because the targeted area included parts of extremities. In summary, respiratory signal extraction with torso localization effectively reduces the interference caused by the extremities movement, and the accuracy of respiratory signals were less varied across subjects.

4.4.3.4 Respiration in Tilted Bed Environments

Another common scenario of sleep environment in clinics is a tilted bed setup. Tilted bed environments change the original pressure distribution underneath a human body. Hence, it is necessary to evaluate the effect of a tilted environment on respiratory signal extraction. Figure 4.10 shows pressure image samples from a tilted environment with raised head (15°), raise knee (15°), and both raised

Table 4.4: Results show how the region of extracted data affects the quality of breath counts. This table shows the difference in counts between estimated breathing and the ground truth over 10 minute periods. The recordings contain 160-180 breaths. Three regions of feature extraction are tested and the torso region shows the least error.

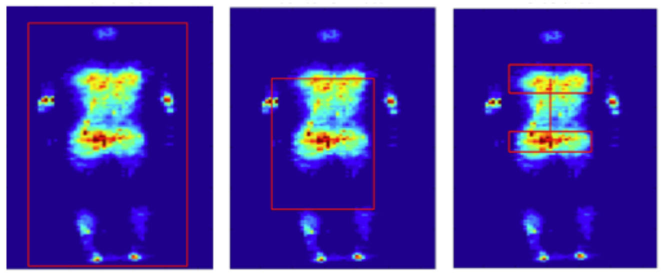

ID	Fullsheet	Center of Mass	Torso Area
1	11	10	2
2	14	9	4
3	-8	-6	-3
4	-8	-4	-1
5	12	8	3
6	-7	-2	-2
7	6	1	3
8	-6	-5	-3
9	11	9	4
10	8	8	2
11	4	5	3
12	-9	-7	-2
Ave.	**9.18**	**6.67**	**2.79**
Error	**5.7%**	**4.1%**	**1.7%**

head and knee. Although pressure distribution changed with degree of tilting, the areas of chest and stomach were still visually recognizable. Pressure redistribution caused by a tilted bed environment has limited effect on body contact area size and the pressure values in chest and hips areas are still prominent compared to other regions. However, the major difference is the distribution of pressure within the body profile.

In this experiment, participants were requested to lie in supine position for 5 minutes of recording. Results of Figure 4.11 reveal that respiratory signals can be extracted from a tilted bed environment and show consistency. Actually, it is worth noticing that much under body pressure was accumulated in the chest area for the case of raised knee tilting; hence, the interference caused by the upper extremities movements had larger weight in the vertical weighting calculation. On the other hand, much under body pressure was accumulated in the stomach and hip area for the case of the raised head tilting; hence, the interference caused by the lower extremities movements had larger impact on the respiratory signals extraction. Therefore, torso localization becomes more important in a tilted bed environment because redistributed pressure tends to increase the weight of extremity movements. Slight extremities movement may incur large interference to respiratory signal extraction.

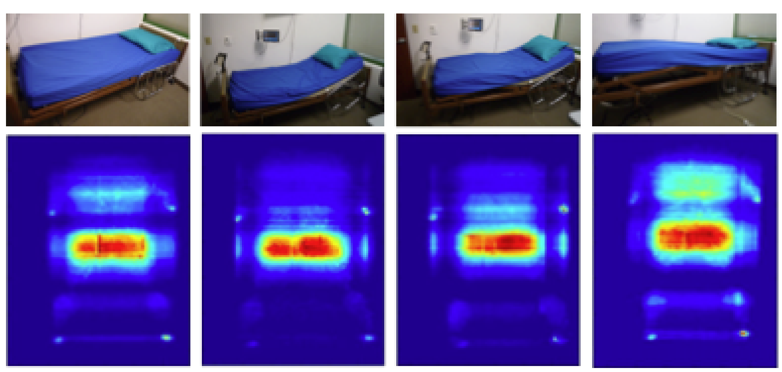

(a) Original (b) HeadLift (c) EndLift (d) BothLift

Figure 4.10: Tilted Bed Setup

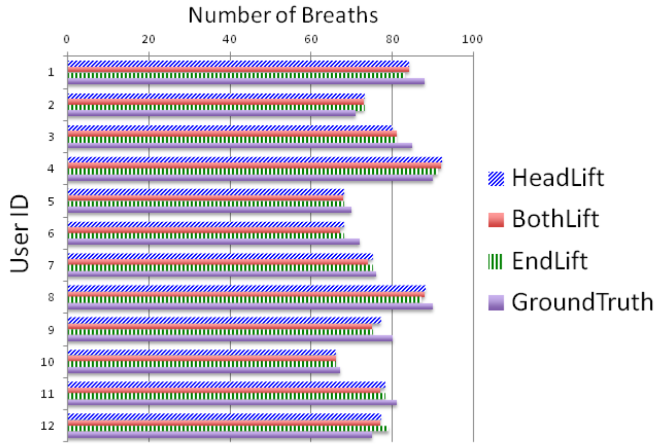

Figure 4.11: Breath count comparison for each subject on tilted beds

4.4.4 Conclusion

In this work, a continuous and unobtrusive system that monitors on-bed respiration using a high density pressure bedsheet is presented. The experimental results show that breathing events are accurately identified in several different situations. All sleep movements are recorded as pressure images detected by the e-Textile bed sheet and are analyzed via pressure images analysis, namely torso localization, respiration signal extraction and peak detection. The complete system design can promote clinical or at-home sleep condition monitoring and assist in notifications due to possible breathing-related disorders. It could be used for situations such as sleep apnea screening to alert for possible medical diagnoses.

CHAPTER 5

Dynamic Motion Recognition

5.1 Background

This chapter deals with recognizing physical motion on the pressure sensor. In general, classifying human action just using pressure images is difficult, so the motions that are studied in this chapter are limited to physical rehabilitation exercises.

Zhou and Hu's survey [ZH08] of human motion tracking systems for rehabilitation targeted primarily stroke sufferers, but this list of technological approaches can be applied to rehabilitation in general. Specialized exercise equipment, such as treadmills, or even robotic guidance devices [KVA00] have been investigated for strength building applications. In addition, visual tracking of body posture has undergone much research, however many relied on marker systems placed on the body [TH03]. Furthermore, marker-free systems try to overcome these limitations by building 2-D [FB02] or 3-D models of the human body [DF01]. Other non-visual methods have been researched, such as using inertial sensors [JMO05]. Combination of sensors are also described, such as Huang's et al. work with inertial sensors and visual camera that tracked both (fine-grain) finger and (course-grain) hand movements for upper extremities rehabilitation [HXS12]. These systems require extensive deployment or calibration and can be inconvenient for the users.

This work focuses on rehabilitation monitoring of subject motions and posture changes, and in particular, with patients who are bed-ridden or restricted

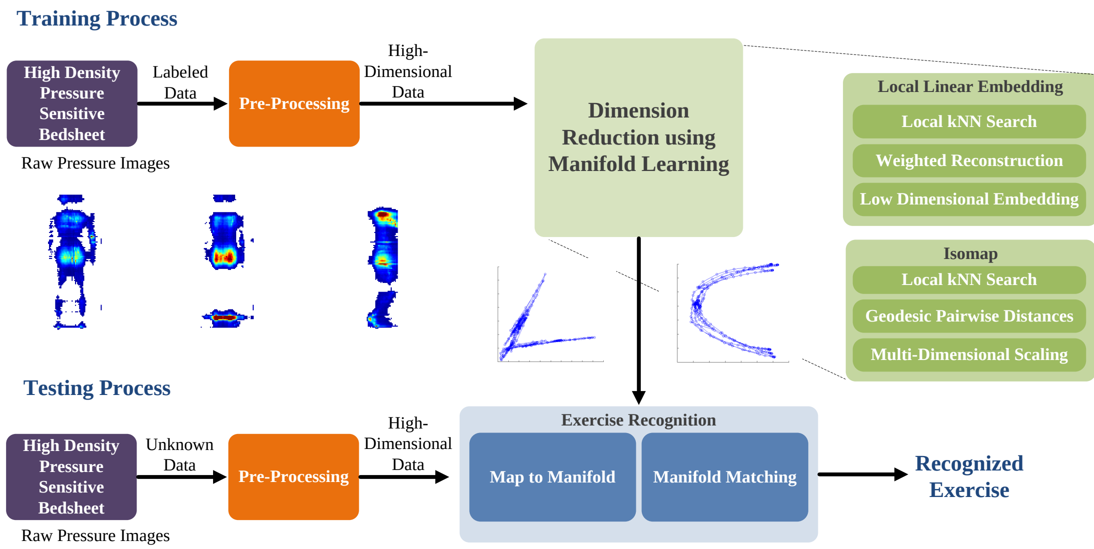

Figure 5.1: Process Flow for On-bed Exercise Monitoring

to motions on bed. There are current research approaches that focus on posture change detection, such as research by Nakajima et al. in which real-time video image sequences were used to extract optical flow information [NMT01]. Jones et al. used a 24 pressure sensor array to identify posture movement times and then evaluated sleep restlessness [JGK06], while Adami et al. used 4 load cell sensors with 200Hz sampling rates to analyze time varying waveforms as patients move on bed [APH10].

Accurate detection of posture movement are shown in these previous methods. They are able to show the existence of posture changes, but they do not target the recognition of actual posture. A system to detect transitions between sitting and lying postures using large pressure sensor arrays placed under the mattress was developed by Foubert et al. [FMG12]. Yousefi et al. were successful in recognizing sleep posture using principle component analysis (PCA) [YOF11], while Hsia et al. used statistical feature extraction [HHC08]. Harada et al. investigated body posture tracking and used generative models of human body pressure to match the patient's pressure distribution [HSM00]. Most related studies used a very limited number of sensors for measuring pressure distribution and do not report any dynamic on-bed motion results. There are no similar type of on-bed exercise monitoring methods with which to compare the following results.

5.2 Algorithmic Framework for Exercise Monitoring

Figure 5.1 introduces the three main steps, and this process is described in more detail in the following section.

- Step 1: Pre-processing of the pressure image
- Step 2: Dimension reduction via manifold learning
- Step 3: Activity recognition using manifold matching.

Exercise recognition uses a subject's pre-recorded training data to match exercises under test. The training data consists of samples of on-bed exercises that are analyzed to produce a low dimensional representation, i.e., a manifold, from the original high resolution pressure images. When new exercise data is recorded, it is mapped to the same low dimensional manifold representation and matched to the closest training exercise manifold.

5.3 Pre-processing

The pre-processing of the raw pressure images is required so that the image sequences can be standardized in such a way to enable successful recognition. The raw images contain noise and artifacts that affect recognition performance, and pre-processing mitigates the side effects as much as possible.

Firstly, the subject can be located anywhere on the bedsheet, so to correct this, the images are aligned to a common center of mass and relocated to the center of the image. A smoothing filter of a symmetric 5×5 unit normal distribution is applied. This smoothing minimizes the effect of noise in the pressure map. The images are normalized so that the sum of pixel weights is one. This step attempts to counteract the effects for different body mass.

5.4 Dimension Reduction using Manifold Learning

In general, image analysis on raw high dimensional data is computationally expensive, so dimension reduction techniques are usually applied to transform the data into another domain to either make it more manageable or useful for further analysis. Principle Component Analysis (PCA) is a well known method of dimension reduction and has widespread use in applications such as face recognition, speech analysis, and medical classification. PCA finds the principle components, i.e., the main orthogonal base axes with which each data sample can be linearly constructed. The result is that only a subset of base axes are required to sufficiently represent the original data.

In this work, two other methods of dimension reduction are investigated: Local Linear Embedding (LLE) and Isomap. Both of these are manifold learning types of dimension reduction. The advantage of manifold learning techniques is that they can find the underlying structure, or the manifold, and can be visualized if the inherent dimension is low enough.

5.4.1 Local Linear Embedding

The first method to map the image sequence X to a low dimensional space is based on the Local Linear Embedding (LLE) framework by Saul and Roweis [SR03], which has various applications in machine learning systems [LXH12]. LLE is an unsupervised algorithm that reconstructs the global data non-linearly while preserving local linearity. After the computation, similar images will be clustered within the low dimensional manifold. In general, there are three steps in the algorithm, which will be described in the following.

5.4.1.1 k-Nearest Neighbor Searching

The first step is to search k-nearest neighbors for each image. In the searching process, Euclidean distance is used to evaluate the similarity between images. For this work, the 30 nearest neighbors of each image are used.

5.4.1.2 Weighted Reconstruction With Nearest Neighbors

The second step is to reconstruct a sample image using its nearest neighbors. Assume that an arbitrary image x has k-nearest neighbors x_i. Then x can ideally be represented as a linear combination of its neighbors. In general, an exact reconstruction will not be found, so a reconstruction error e for a single sample x can be formulated as:

$$e = \|x - \sum_{i=1}^{k} w_i x_i\|, \tag{5.1}$$

where w_i denotes the reconstruction weight for the neighbor x_i.

For N images, the total error is:

$$E = \sum_{j=1}^{N} \|x_j - \sum_{i=1}^{N} w_{ij} x_{ij}\|, \tag{5.2}$$

where each x_j is an image. x_{ij} is the ith neighbor of x_j, and w_{ij} is the reconstruction weight for x_{ij}. The optimization process minimizes the reconstruction error of all images by finding appropriate values for the weights w_{ij}. There are two attributes of the problem to ensure it is well-imposed: (1) exclusiveness: the weight w_{ij} is zero if x_{ij} is not in the nearest neighbor list of x_j; (2) normalization:

the sum of the weights of nearest neighbors of x_j should be 1. Equation (5.2) has a closed least square solution and the weights w_{ij} can be solved efficiently [SR03].

5.4.1.3 Low Dimensional Embedding Construction

The third step is to construct the corresponding embedding in a low dimensional space. Based on the calculation results from the second step, the intrinsic geometrical structure of each local cluster is characterized by w_{ij}. It is assumed that the neighborhood relation in high dimensional space should be preserved in low dimensional space, i.e., within a manifold. Based on this assumption, the embedding process finds the low dimensional representation y of x by minimizing the following error E':

$$E' = \sum_{j=1}^{N} \|y_j - \sum_{i=1}^{N} w_{ij} y_{ij}\|, \tag{5.3}$$

where y_j and y_{ij} are the corresponding points of x_j and x_{ij} in the low dimensional manifold. It is noted that Equation (5.3) is in a quadratic form and the embedding optimization process is efficiently solvable. Furthermore, all the manifold points y_i will be computed globally and simultaneously, and no local optima will affect the construction result.

Equations (5.2) and (5.3) indicate that the low dimensional construction is only based on the local neighborhood data. This means that the computed manifold y_i can be translated with an arbitrary displacement. Moreover, LLE states the computed manifold y_i can be rotated by an arbitrary angle without affecting Equation (5.3) too. These geometric attributes can be represented and formulated with the following two constraints:

$$\sum_{i=1}^{N} y_i = 0, \quad \frac{1}{N} \sum_{i=1}^{N} y_i \cdot y_i = 1. \tag{5.4}$$

Therefore, manifold construction problem becomes an eigenvalue problem [SR03], in which the matrix rank is selected to have the desired manifold dimension.

5.4.2 Isomap

The second method to map the image sequence X to a low dimensional space is based on the Isomap framework by Tenenbaum et al. [TSL00]. Isomap also performs non-linear dimension reduction and extends the classical linear Multi-dimensional Scaling (MDS) method [KW78]. MDS finds a set of co-ordinates that satisfies given pairwise distances between points. However, given that the points may lie on a manifold inside a high dimensional space, linear pairwise distances may not represent the true structure.

5.4.2.1 k-Nearest Neighbor Searching

This stage is similar to LLE where k-Nearest Neighbors for each original image are selected using the Euclidean distance in high dimensions.

5.4.2.2 Computation of Geodesic Pairwise Distance

The distances between all pairs of images are estimated given the distances between local sets of images. This results in the geodesic pairwise distances, i.e. the shortest path distances D_{ij}^X along a curved surface. Floyd's algorithm can be used to find the shortest paths between every pair of images in a graph, or other faster methods [KGG94].

5.4.2.3 Low Dimensional Embedding via Multi-Dimensional Scaling

The final stage of Isomap applies the regular MDS algorithm to the geodesic distances. MDS finds points Y that minimize the total error between pairwise distances in high dimensional space and pairwise distances in low dimensional space:

$$\min_{Y} \sum_{i=1}^{N} \sum_{j=1}^{N} (D_{ij}^X - D_{ij}^Y)^2, \tag{5.5}$$

where D_{ij}^Y is the pairwise distance between points in the low d-dimensional space Y. The low dimensional embedding is solved by taking the co-ordinates of the top d eigenvectors of the inner-product matrix of the geodesic pairwise distances [KW78].

Contrasting with LLE, Isomap preserves pairwise distances within the manifold, while LLE preserves the local linear structure within the manifold.

5.5 Exercise Recognition using Manifold Matching

5.5.1 Map input to manifold

Once the training data has been reduced in dimensionality to its corresponding low dimensional form, the process is evaluated using new test data against the training data. The testing data needs to be converted into manifold form. Note that it is possible to run the whole LLE or Isomap algorithm again on the combined testing data and training data in order to find the low dimensional representation of the test data, however this is not necessary.

Instead, a portion of the algorithm needs only to be executed [SR03, ZS11]. Given a new test image $\hat{x}$, the goal is to find its low dimensional representation, $\hat{y}$. To do so, the weights w_i are computed from the k nearest neighbors of $\hat{x}$ in the training set, x_i. This is again the least squares solution to minimize

$$\|\hat{x} - \sum_{i=1}^{k} w_i x_i\|, \tag{5.6}$$

with the constraint $\sum_{i=1}^{k} w_i = 1$. Since the corresponding low dimensional co-ordinates of x_i are known during the training phase, the resultant embedded

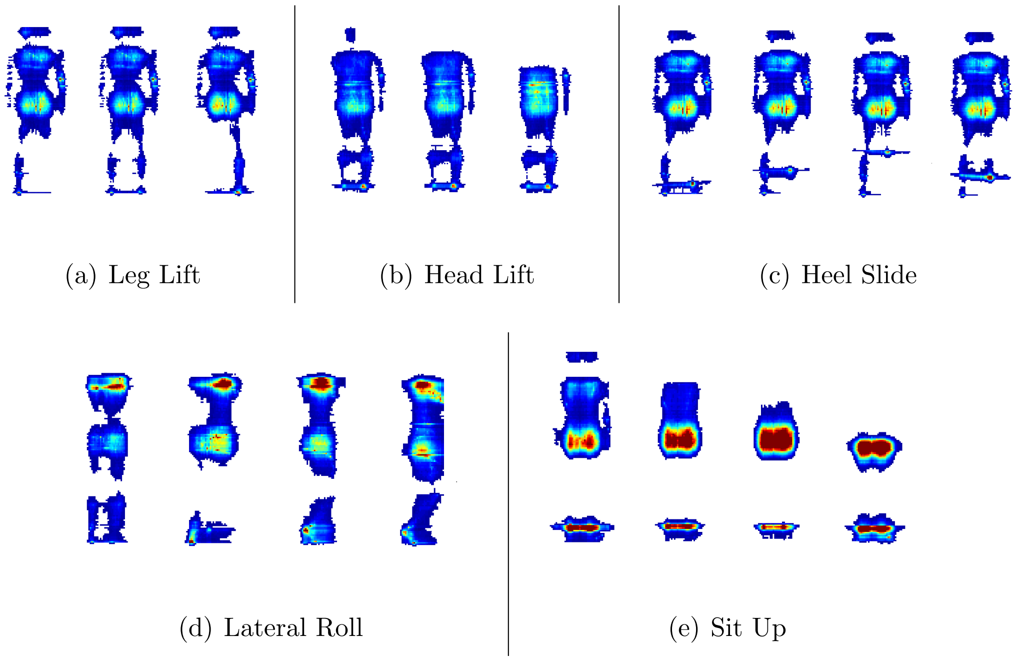

(a) Leg Lift (b) Head Lift (c) Heel Slide

(d) Lateral Roll (e) Sit Up

Figure 5.2: Sample Images

co-ordinates for $\hat{y}$ are constructed using the same weights:

$$\hat{y} = \sum_{i=1}^{k} w_i y_i, \tag{5.7}$$

where y_i are the corresponding embedded points of x_i.

5.5.2 Manifold Matching

Exercise tracking involves checking how well the testing data follows the trajectory of a given exercise manifold. The trajectories are compared using a similar idea to the Hausdorff distance. The distance of a point to a manifold is equal to the shortest Euclidean distance to any point in the manifold. The similarity of two manifolds is the mean of the point distances of all the points of one manifold, M_1 to the other manifold, M_2. This is expressed as

$$s(M_1, M_2) = \frac{1}{T_{M_1}} \sum_{i=1}^{T_{M_1}} \min_{1 \leq j \leq T_{M_2}} \|M_1(i) - M_2(j)\|, \tag{5.8}$$

where T_{M_1} and T_{M_2} are the number of points in each manifold. This metric allows manifolds of different lengths to be compared since different subjects take different times to perform each activity. Since the Hausdorff metric is not symmetric, the following sum for the manifold matching metric is given,

$$d(M_1, M_2) = s(M_1, M_2) + s(M_2, M_1). \tag{5.9}$$

So, to measure how well a subject adheres to the prescribed exercise, the testing data is mapped to corresponding low dimensional embedding points that defines a manifold, then the manifold is measured against the expected exercise manifold.

Figure 5.3: Example of Leg Lift Exercise

5.6 Experiments and Discussion

5.6.1 Experimental Setup

This framework for exercise monitoring is evaluated on 10 subjects, 7 male subjects and 3 female subjects. The weight of the subjects ranged from 50kg to 85kg, and height between 155cm and 188cm. There were 5 selected on-bed exercises: alternating Leg Lifts (LL), Head Lifts (HL), alternating Heel Slides (HS), alternating side-to-side Lateral Rolls (LR), and Sit-Ups (SU). These exercises have been selected as being appropriate for on-bed monitoring [NW06]. In the training data collection, at least 5 sets of image sequences were recorded for each of the 5 on-bed exercises for each subject, so there were more than 250 exercise sequences under test. Each image sequence comprises one *exercise activity*, e.g., one Leg

Lift exercise activity includes lifting of the right leg followed by the left leg. The order of left and right does not matter in this system. Each image sequence of exercise activity contained at least 40 individual images. Small variations in body, arm and leg positions were allowed for each subject as only gross motor functions would be analyzed. Examples of exercise and sample images are shown in Figures 5.2 and 5.4.

Table 5.1: Confusion Matrix LLE

	LL	HL	HS	LR	SU	Recall
LL	42	4	6	0	0	80.8%
HL	9	42	2	0	0	79.2%
HS	7	0	54	0	0	88.5%
LR	0	0	0	50	0	100%
SU	0	0	0	1	56	98.2%
Precision	72.4%	91.3%	87.1%	98.0%	100%	

Table 5.2: Confusion Matrix Isomap

	LL	HL	HS	LR	SU	Recall
LL	45	3	4	0	0	86.5%
HL	7	44	2	0	0	83.0%
HS	6	1	54	0	0	88.5%
LR	0	0	0	49	1	98.0%
SU	0	0	0	3	54	94.7%
Precision	77.6%	91.7%	90.0%	94.2%	98.2%	

The training data for each subject was combined and manifold learning was applied to generate the training manifolds for the exercises. Testing was carried out by exercise activity and repeated for each of the exercise activities.

Figure 5.4: Example of Heel Slide Exercise

5.6.2 Experimental Evaluation

Manifolds within high dimensional space exist because similar patterns that correspond to exercises trace similar paths. Distinguishing between different exercises is possible since the corresponding low dimensional manifold representations exhibit different paths. Due to the smooth body pressure transformations in the image sequences, manifold learning methods such as LLE and Isomap are able to produce low dimensional reconstructions of the data points. Manifold learning is well suited to this type of exercise recognition application because human body motion is somewhat limited on-bed and there are only slight variations in posture changes across different subjects.

Tables 5.1 and 5.2 show recognition results for the 5 exercises in 10 subject dependent testing, i.e., subjects are not tested with training data from other subjects. Notably, the highest recognition rates are Lateral Rolls and Sit Ups. This can be expected since these exercises involve the greatest physical exertion and hence the greatest pressure image differences. The other three exercises exhibit a comparably lower rate of recognition due to more of a fine grain difference in the pressure image sequences. The confusion matrix shows that there are the most misclassifications between Leg Lifts vs. Head Lift, followed by Leg Lifts vs. Heel Slides. The former observation is explained by similar muscular pressure that is required when lifting one's head and legs, in that more pressure is added in the back region. As to the latter, there are clear similarities in the pressure images of Figure 5.2, and the leg positions only constitute minor variations in the overall pressure maps.

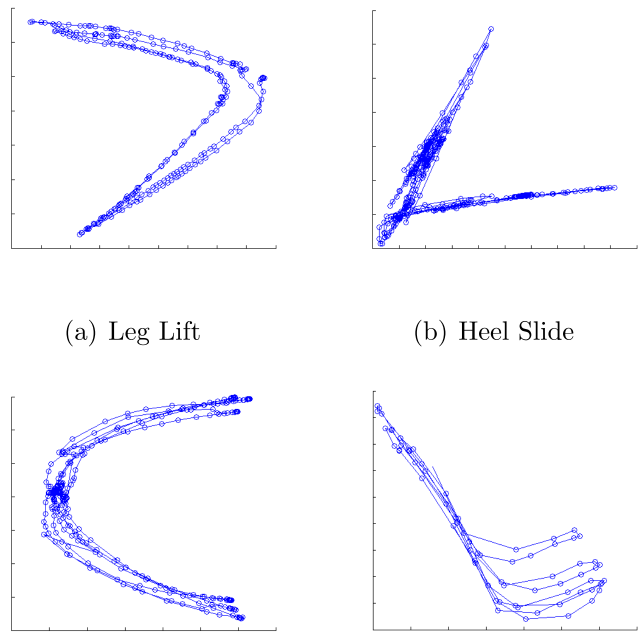

(a) Leg Lift (b) Heel Slide

(c) Lateral Roll (d) Sit Up

Figure 5.5: Samples of Exercise Manifolds LLE

Figure 5.5 shows samples of the low dimensional visualization of manifolds for some of the exercises. Generally the shapes of the manifolds give an indication of the differences between the exercises. It is interesting to note in Figure 5.5(d) that the variations in Sit Ups can be seen. Using the Manifold Matching method, a quantified measurement of exercise recognition is performed.

5.6.3 Comparing LLE and Isomap

The accuracy results between LLE and Isomap are somewhat similar as shown in Tables 5.1 and 5.2. LLE has higher accuracy for the Lateral Rolls and Sit Ups, while Isomap shows higher accuracy for Leg Lifts, Head Lifts and Heel Slides.

Figure 5.6 shows samples of how head-lifts appear on a leg-lift manifold under

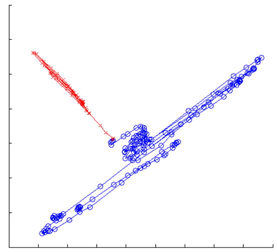

(a) Leg Lift (blue) vs Head Lift (red)

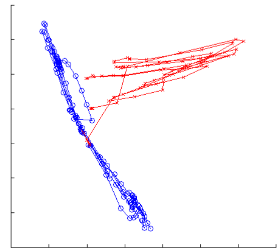

(b) Roll (blue) vs Sit up (red)

Figure 5.6: Samples of Exercise Manifolds LLE

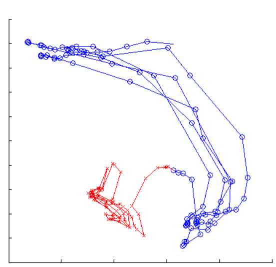

(a) Leg Lift (blue) vs Head Lift (red)

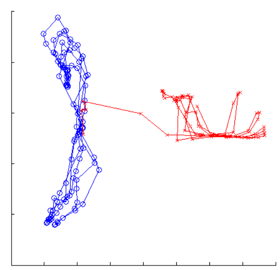

(b) Roll (blue) vs Sit up (red)

Figure 5.7: Samples of Exercise Manifolds Isomap

LLE, and sit-up compared to lateral rolls. Figure 5.7 shows the same results for Isomap. It is evident that the sample exercises can be discerned from each other. It is interesting to note that the manifold shapes produced by Isomap tend to be more variable, which may contribute to the slight variation in accuracy levels.

The dimension reduction algorithm requires the data to be non-sparse, i.e., there must be sufficient sampling of pressure images to track motions. The current state of technology for pressure images of this resolution are 2-5 samples per second. Higher sampling rates can be achieved with the loss of image resolution, i.e., more images can be sampled per second but with lower pixel resolution.

To verify that manifold learning is an appropriate method for exercise recogni-

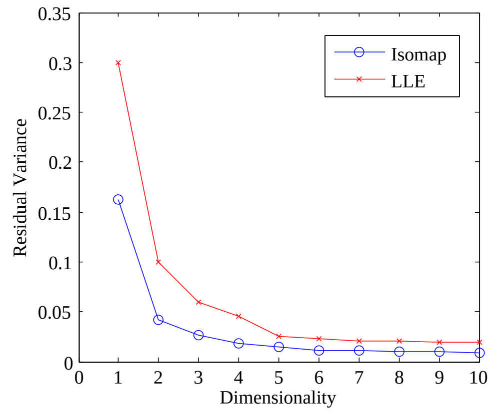

Figure 5.8: Intrinsic Dimensionality of the manifolds are found at the knee points of the graph.

tion, the number of intrinsic dimensions is investigated, i.e., how many variables are sufficient to describe the changes in the data. Figure 5.8 suggests that the intrinsic dimension of the rehabilitation exercise data is 2. In the dimensionality graph, this is seen at the knee point, i.e. where the curves have the largest break. As the dimensionality of the reconstruction space is reduced, the reconstruction error or residual variance slowly increases until dimension 2. A single dimension is clearly not sufficient as it produces large reconstruction errors.

5.6.4 Sequential Evaluation

As a further evaluation of this framework for exercise recognition, a longitudinal study of continuous monitoring through a number of set exercise activity programs is investigated. More specifically, each of the 5 exercises was performed sequentially to analyze whether the algorithm can separate and recognize the exercises. The order of exercises was chosen arbitrarily and it is not atypical in rehabilitation therapy. Figure 5.9 shows the evaluation results of this experiment, where red dash line represents the ground truth, and blue line represents the classification results. It can be seen that 3 sets of 5 different exercises are performed sequentially in this evaluation, and finally 13 out of the 15 exercises are recognized correctly.

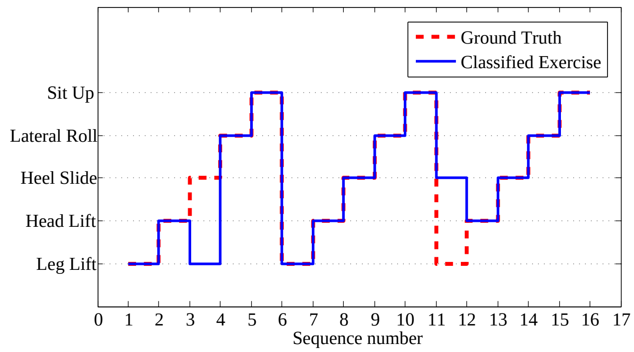

Figure 5.9: A set of 15 exercise activities performed sequentially against ground truth

5.7 Conclusion

In this work, an on-bed exercise monitoring system design which enables caregivers to track compliance to physical rehabilitation programs, is presented. A novel use of dimension reduction techniques from pressure images is employed to find intrinsic subspace representations of the data. A metric to match manifolds is evaluated for quantified measurement of adherence to prescribed exercises.

Future work involves quantifying the performance of a given exercise with respect to standard exercise models, i.e. how closely is the patient following the exercise patterns such as angle of Leg Lifts and length of Heel Slide. Other future endeavors includes facilitating a system to work on chairs for sitting rehabilitative exercise, not only in clinical rooms or home-base care but also for cars or wheelchairs. 3D model reconstruction of patients from 2D pressure images is another goal that can be accomplished using the results of this research work.

CHAPTER 6

Sensing Strategy for Pressure Distribution

6.1 Introduction

The question is posed: do all pixels need to be sampled in order to make accurate predictions? If only a portion of the image is sampled, can a reliable reconstruction be produced?

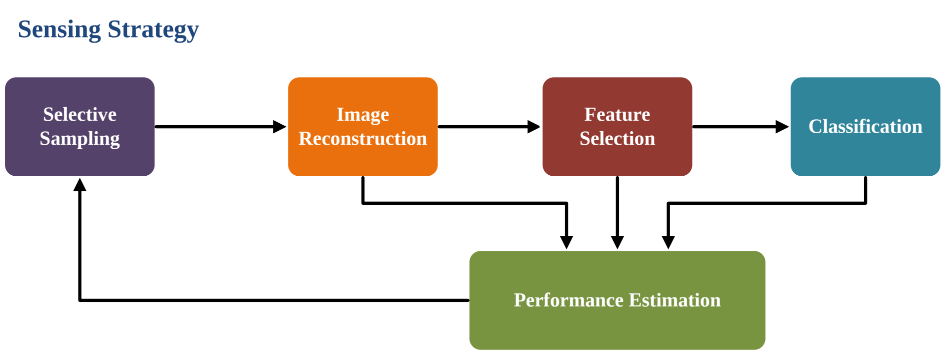

Figure 6.1: Overview of Sensing Strategy Framework

In this section, a proposed energy-efficient adaptive sensing framework is explored. Fig. 6.1 shows the scheme overview. These are the new components in this framework: Selective Sampling, Reconstruction, and Performance Evaluation. The other two components of Feature Selection and Classficiation have already been discussed in the previous chapters. At each stage, the performance of the method is updated and then feeds back into a change in the sampling strategy to allow the constancy of classification accuracy.

6.2 Local Randomized Selective Sensing

The first step is selective sampling from the dense pressure sensor array. The goal of selective sampling is to reduce the number of samples per frame in order to use these limited sensor measurement points to estimate the entire pressure image. From Chapter 3, the system identifies which posture the subject is in and then is able to apply a two-fold sampling strategy. Firstly, the samples are selected randomly and sparsely. Secondly, the sparse sampling is limited to regions around predefined locales based on the posture. The process is described here.

For one pressure image frame, consider an image x as a N pixel vector in $\mathbb{R}^N$, i.e. the two dimension image is unfolded into a single column vector. This image x can be represented as a matrix form:

$$x = Ix, \tag{6.1}$$

where I is the $N \times N$ identity matrix.

Row-wise swaps on the identity matrix are performed to convert I to A so that A is a randomized permuted version of I:

$$A_{N\times N} = \begin{bmatrix} 0 & \cdots & \cdots & \cdots & 1 & \cdots & 0 \\ 0 & \cdots & 1 & \cdots & \cdots & \cdots & 0 \\ \cdots & \cdots & \cdots & \cdots & \cdots & \cdots & \cdots \\ 0 & \cdots & \cdots & 1 & \cdots & \cdots & 0 \end{bmatrix}, \tag{6.2}$$

Now y is informatively equivalent to x in

$$y = Ax. \tag{6.3}$$

When the top k rows, A_k, of A are selected to construct y, denoted as y_k, it is:

$$y_k = A_{k\times N}x. \tag{6.4}$$

From now on, one can refer to k as the selective sampling ratio compared to the full number of sensors. It can be seen that y_k is not informatively equivalent to the original x since $N-k$ sensor values are missing. $A_{k\times N}$ is called the selective sensing matrix, and y_k is the selective sensing output. This process describes how the random selection of samples is made. The only update that is needed to restrict the sampling to localized regions is to predefine the allowable permutations of rows of A, i.e. only certain rows of A are allowed to be swapped. This ensures that the top k rows will be sampled from the specific regions. Note that the value of k will be set according to the different postures.

6.3 Sparsity-Based Reconstruction

This section discusses how to use y_k to reconstruct x. The reconstruction method is based on the theory of sparse representation (SR). Sparse presentation has been successfully applied to signal reconstruction, i.e., in Compressed Sensing [Don06]. Note that one must maintain a distinction between the term *sparsity* and the term *selective sampling*. Selective sampling means the reduction in the number of measured samples, while sparsity refers to the low number of dimensions in which the data can be represented. In Compressed Sensing, $x \in \mathbb{R}^N$ is a vector of unknown variables, and $y \in \mathbb{R}^k$ is the limited measurements through $A \in \mathbb{R}^{k\times N}$. A is typically either a random Gaussian or Bernoulli matrix. So:

$$y = Ax, \tag{6.5}$$

Since k is less than N, Eq. (6.5) becomes an underdetermined system, and x can not be uniquely reconstructed. However, if x is a structural signal, it should be sparse under some transformation Ψ, i.e., $x = \Psi z$, where $z \in \mathbb{R}^N$ is sparse. In this way, x can be reconstructed with the l_0 minimization formulation:

$$\begin{aligned} &\min\nolimits_z ||z||_0 \\ s.t. \quad &y = A\Psi z. \end{aligned} \tag{6.6}$$

With Eq. (6.6), there are two questions here. The first question is how to find the transformation Ψ such that z is sparse. In this application, considering x is a pressure image measurement, the direct cosine transform (DCT) is employed to represent the unknown x.

The second question is how to solve this formulation. Eq. (6.6) is a determined system and has stable solution. However, Eq. (6.6) is an intractable NP-hard problem [Nat95]. There are two ways to estimate Eq. (6.6). One is to convexify the formulation with the l_1 minimization [CRT06]:

$$\begin{aligned} &\min\nolimits_z ||z||_1 \\ s.t. \quad & y = A\Psi z. \end{aligned} \tag{6.7}$$

However, solving the l_1 minimization is time-consuming and not scalable [CRT06]. The other method uses heuristic algorithms to approximate the solution of l_0 directly. One of the popular methods is Orthogonal Matching Pursuit (OMP) [PRK93]. OMP, being a greedy algorithm, has advantages in speed and ease of implementation [TG07]. If one considers $A\Psi$ as a matrix Θ, then the sparsest solution z can be found that combines with the columns of Θ to give y. Another way to view this is that the sparse solution is the same solution that would result from a reduced set of columns, say Θ_t. OMP finds these columns, or bases, in order by choosing a column of Θ that most closely resembles y and subtracts off its contribution from y for the next iteration. The details of OMP is described in Algorithm 2.

In more detail: The initialization step sets a residual $r_0 = y - \Theta_t z_t = y$ for time $t = 0$. At iteration t, Step 2 finds the column θ_t that maximizes its inner product with r_{t-1} for $j = 1..N$. This column is the most similar to the residual r_{t-1}. Step 3 adds this column vector θ_t to a matrix of chosen bases Θ_t, where Θ_0 was initialized as an empty matrix. Step 4 finds a t element solution of the system using only t columns. Since t is less than k, the solution can be found by least squares. Step 5 calculates new approximations of the residual. z_t is the solution of z with the most representative columns of Θ. The residual is always orthogonal

Algorithm 2 The Orthogonal Matching Pursuit Algorithm

Input: $y \in \mathbb{R}^k$, $A \in \mathbb{R}^{k\times N}$, $\Psi \in \mathbb{R}^{N\times N}$;

Output: $x \in \mathbb{R}^N$;

/* Initialization */

Step 1: $\Theta = A\Psi$, $r_0 = y$, $\Theta_0 = \emptyset$, $t = 1$.

/* Iteration */

Step 2: $\theta_t = \arg\max_{\theta_j} |r_{t-1}.\theta_j|, j = 1..N$.

Step 3: $\Theta_t = [\Theta_{t-1}, \theta_t]$.

Step 4: $z_t = \arg\min_z ||y - \Theta_t z||_2$.

Step 5: $r_t = y - \Theta_t z_t$.

Step 6: if $\|r_t\|_2 < \varepsilon$, stop,

otherwise $t = t + 1$, go to Step 2.

/* Output */

Step 7: $x = \Psi z_t$.

to the chosen bases Θ_t, which results in a zero correlation between residual and any of these bases and so future iterations will never choose a previously selected column. This continues until a stopping criterion is met. Finally, Step 7 gives the reconstructed solution for x where z_t is transformed by Ψ.

6.4 Experiments

This section discusses the evaluation of the proposed method of signal reconstruction with variation in sampling density. In brief, it demonstrates that the method of selective sampling is able to reconstruct the original raw pressure maps with minimal loss of accuracy.

Firstly, *two* metrics to quantitatively measure the reconstruction errors are declared:

- NMSE: Normalized Mean Square Error is given by
$$\frac{||x - \hat{x}||_2^2}{||x||_2^2},$$
where x represents the original signal, and $\hat{x}$ is the reconstructed image of x. NMSE is between 0 to 100%, and it has been widely applied to error quantization in various signals, such as time series [Wei94] and images [WBS04].

- SSIM: Structural SIMilarity (SSIM) is often considered a better visual estimator of spatially structural signal similarity, such as images, than NMSE [WBS04]. The main premise is that structural information of image pixels have strong inter-dependencies especially when they are spatially close. The SSIM metric ranges between [-1.0,+1.0] where +1.0 means tested images are identical.

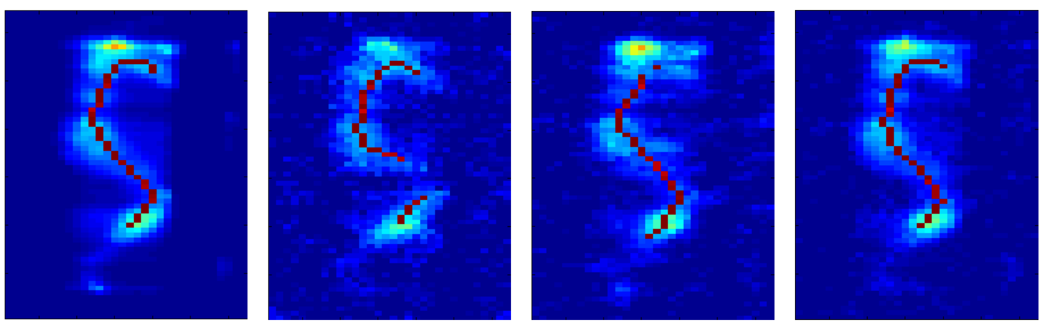

(a) Original (b) 20% (c) 30% (d) 40%

Figure 6.2: Reconstructed pressure images from sparse sampling.

Fig. 6.2 shows the original pressure image from a sample lateral posture, reconstructed images using 20%, 30%, and 40% of sensor values randomly selected. The results indicates that the reconstructed image is visually close to the original. It is because the pressure image is intrinsically very sparse under some transform domain (such as DCT in this case), and it is possible to construct the information with limited measurements.

To validate the method of image reconstruction using Sparse Representation, it is compared with simple image interpolation. Fig. 6.3 shows the comparison of

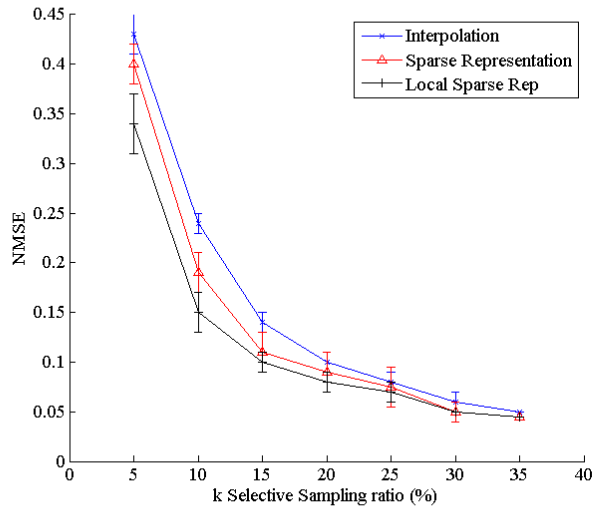

Figure 6.3: Reconstruction error for various k-selective sensing schemes over 300 reconstructed images

reconstruction error for these methods of 300 image frames for selected samples k between 5-35%. Image interpolation calculates the unsampled pixels by taking the average values of horizontal and vertical linear interpolations. For low numbers of selected samples, the result shows that the Sparse Representation method can reconstruct the images slightly better than pixel interpolation. Furthermore, localized sampling with Sparse Representation reduces the reconstruction error compared to the global version of this method.

Figure 6.4 shows that the Prone posture are not reconstructed as well as the lateral postures, while Supine posture has some error in its reconstruction but is not evident in the structural similarity.

6.5 Extension of Sparse Sampling to Gait Analysis

So far this chapter deals with a method of sparse sampling and image reconstruction in order to reduce the number of samples for ideal pressure monitoring. The presented results show that a good reduction in the sampling density allows

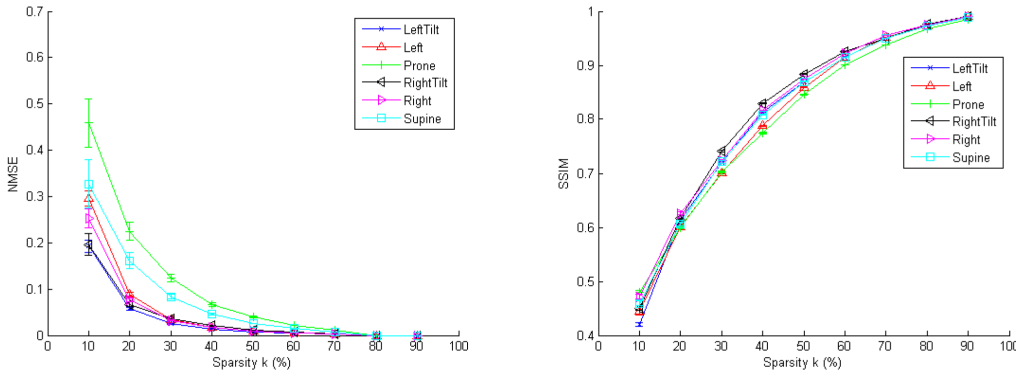

(a) (b)

Figure 6.4: (a) Reconstruction error and (b) Structural similarity for various postures over a range of sparsity.

accurate image reconstruction. As an extension to this method, a theoretical investigation of using a similar pressure sensor in an insole is described in the remainder of this chapter. It seems energy consumption is a main factor in mobile sensing and the application of portable gait monitoring is being widely studied in research labs.

Gait is one of the important characteristics of human locomotion, and gait analysis has been applied in diverse applications in the medical and healthcare domains [GS08]. Especially in elderly healthcare, gait analysis is an important tool to assess fall risk and fall prevention [LSH09, BRN10]. Brand surveyed methods of gait analysis in physical rehabilitation settings for evaluating post-surgical recovery and treatment efficacy [Bak06]. As an example, gait parameters of post-stroke patients were analyzed to evaluate their rehabilitation status [XBW12]. In the fields of orthopedics and prosthetics, gait analysis is essential to quantify gait conditions and assess the applications of orthopedic assistive devices [LJN12].

Gait labs are the traditional environments where medical practitioners observe human gait motions. These controlled systems are equipped with high-speed cameras, pressure sensitive carpets and lighting facilities. In a gait study, the subject will walk with color markers on the body, and these devices will capture the motion and allow extraction of the subject's gait parameters. With the development of wearable sensor systems, it makes sense to move the monitoring outside the lab, where longitudinal gait monitoring can be done in a more comfortable setting. Some examples of recent research work include mobile systems with 3-axis accelerometers and gyroscopes [LIS09]; Bae et al. [BKB09] presented a Force Sensing Resistive (FSR) sensor array based system for gait analysis; and Chen et al. [CCB12] used inertial sensors on cerebral palsy patients for longitudinal motion assessment.

6.5.1 A Smart Insole System

A Smart Insole system can offer high spatial-resolution sensing of plantar pressure from which gait features can be extracted. However, power consumption is the main challenge because of the concentration of sensors. In general, there are two options: either reduce the sampling rate or reduce the sampling density. To this end, an adaptive sensing scheme to reduce the sampling density, as well as control the locality of samples, while preserving information fidelity is explored. To gauge the density of spatial sensor data, the number of sample points needed in the system is reduced. Note that, in contrast to the compressed sensing technology [CRT06], this method can be implemented with the traditional ADC modeling rather than requiring special ADC components. In the reconstruction of the high density image, the proposed method of sparse representation is claimed to be better than simple interpolation especially for low number of samples, as shown in the experimental results.

6.5.2 A Framework for Adaptive Sensing

An energy-efficient adaptive sensing framework for gait analysis is presented. The main components in this framework are pre-sampling and real-time gait analysis, local randomized selective sensing, and sparsity-based signal reconstruction.

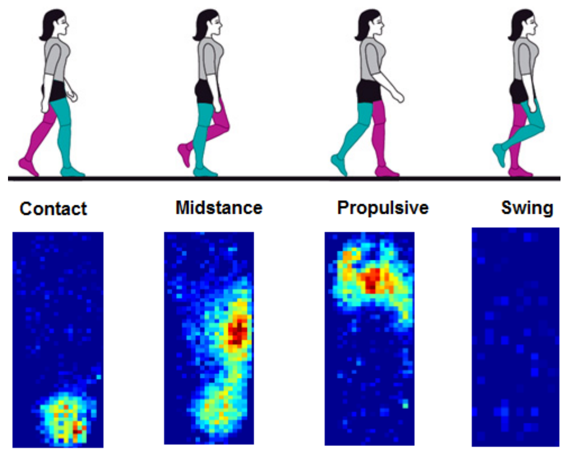

Figure 6.5: Four main stages of the gait cycle

The general idea of adaptive sensing is to change the number of samples for each frame according to the pressure image content. For example, there are four different gait stages in one gait cycle: swing (S), contact (C), midstance (M) and propulsive (P) stage. Fig. 6.5 shows the pressure image in each stage. The pressure distribution on each stage is different, and it can use selected pressure sensors to determine the gait phase. For instance, there is no pressure under the foot in the swing stage, and there is no need to sample the pressure image.

For pre-sampling and real-time gait stage analysis, there are two considerations here. First, the analysis procedure should run in real-time for the sake of high speed sampling. Second, the analysis should be accurate to ensure the correctness of gait stage analysis. In this work, three prominent points in the pressure sensor array are pre-sampled to recognize the gait phases. As shown in Fig 6.6, three positions are at the front, middle and back, respectively. In this way, three easily sampled sensor values are used to gauge the stage phase. A simple comparison of these three selected pressure points with cut-off thresholds is sufficient to identify the gait phase for the purpose of selective sampling. For example, if the back pressure point is greater than its threshold, and both the middle and front pressure points are lower than their thresholds, then the phase is the contact phase. Each of the thresholds is chosen initially from experiments.

The remaining components of local randomized selective sampling and sparsity-based signal reconstruction have been described earlier in the chapter pertaining to the bedsheet pressure analysis.

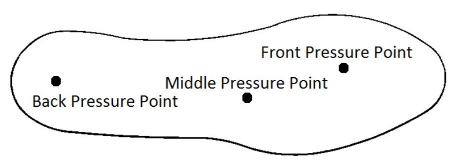

Figure 6.6: Three pre-sampling points

6.5.3 Evaluation and Discussion

This framework was evaluated on three aspects: (1) Evaluation of signal reconstruction with variation in sampling density, (2) Energy efficiency improvement, and (3) Information integrity of gait features. In brief, the first subsection demonstrates that the method of selective sampling is able to reconstruct the original raw pressure maps with minimal loss of accuracy. The second subsection shows the important improvement in energy efficiency by selective sampling and image reconstruction. Then, in the third subsection, the characteristic gait features do not degrade even when only using a subset of data and with lower energy consumption.

6.5.3.1 Evaluation of Signal Reconstruction

The performance on a single pressure image is examined first. Fig. 6.7(a) is the original pressure image from the midstance stage, and Fig. 6.7(b) is the reconstructed image from 25% of sensor values randomly selected. The DCT coefficients of the original and the reconstructed are shown in Fig. 6.7(c) and Fig. 6.7(d), respectively. The results indicates that the reconstructed image is visually close to the original. It is because the pressure image is intrinsically very sparse under some transform domain (such as DCT in this case), and it is possible to construct the information with limited measurements.

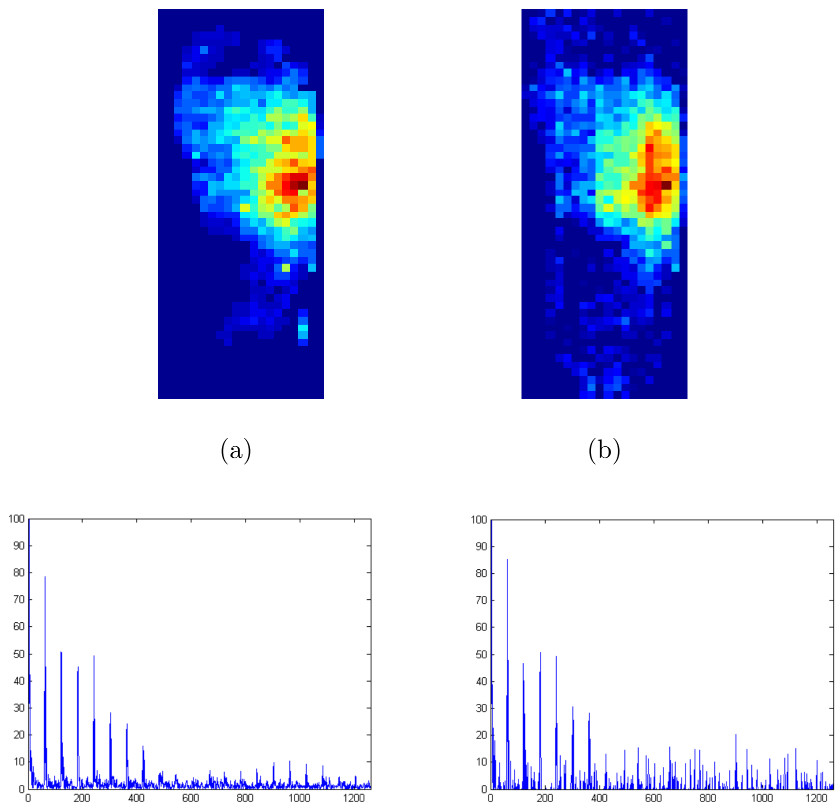

(c) (d)

Figure 6.7: (a) Original image vs (b) reconstructed with k = 25%. Direct cosine transform coefficients for (c) original and (d) reconstructed.

The performance on continuous sensing signal of gait cycle is examined next.

This part uses the data of 5 steps of the right foot, including 500 sequential pressure images. The sample rate of Smart Insole is 30Hz. Fig. 6.8 shows SSIM results in this experiment. The results consist of three curves, which corresponds to the sensing percentage (k) 25%, 50% and 75%, respectively. It is not surprising that the high sensing percentage leads to higher SSIM values. Furthermore, one also sees, under the constant sensing setup, that the reconstruction quality follows some pattern and varies a lot according to different gait stages. More specifically, at the Contact stage, i.e., as the heel touches down, the structural similarity between original and reconstructed images is relatively low (see Fig. 6.8). It rises through the Midstance to a peak SSIM, then lowers until the Propulsive stage, i.e. as the foot pushes off its ball and toes.

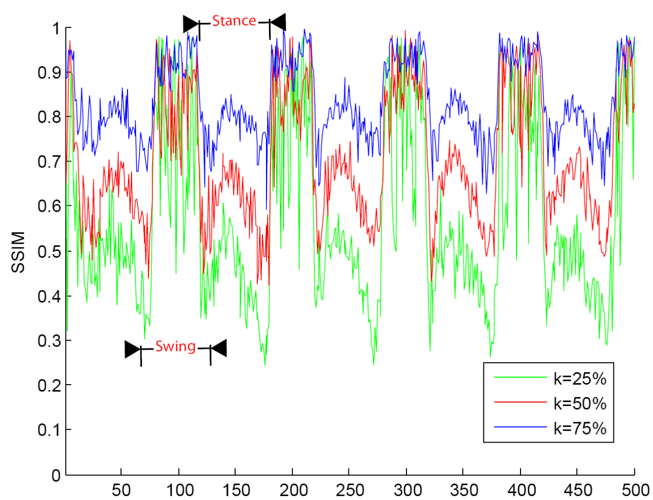

Figure 6.8: SSIM for various k-selective sensing schemes over 500 sequential reconstructed images

Furthermore, the effect of sample number reduction is explored. The setup of SSIM values is fixed and the question of how many samples are required to keep the SSIM values constant is asked. In this experiment, SSIM is set with four different values, including 0.4, 0.5, 0.6 and 0.7. For the clarity of presentation, the data of the stance phase is used from 10 gait cycles and the whole phase is partitioned into ten segments. The results are shown in Fig. 6.9, which illustrates how the value of k-selective sensing setup varies when structural similarity requirement is constant throughout the step cycle. From the mean value curve, one can see that the higher SSIM, the more required samples. Also, the variation pattern of k-selective sensing setup follows the similar trend. More specifically, at the beginning of the step, the value of k is high in order to achieve the required structural similarity to the original image. Toward the middle of the step, the k value can decrease as reconstruction ability improves due to more plantar pressure. Then the k value rises to the end of the step cycle, meaning that more selected samples are required to reach the same level of reconstruction quality. The start and end phases of the step have less structural information in the visual image and so a higher number of selected samples are needed. Note that the standard deviation at the beginning stage is large, and progressively becomes smaller. The observation indicates the large variation of pressure distribution on the heel strike, which can be considered in future work.

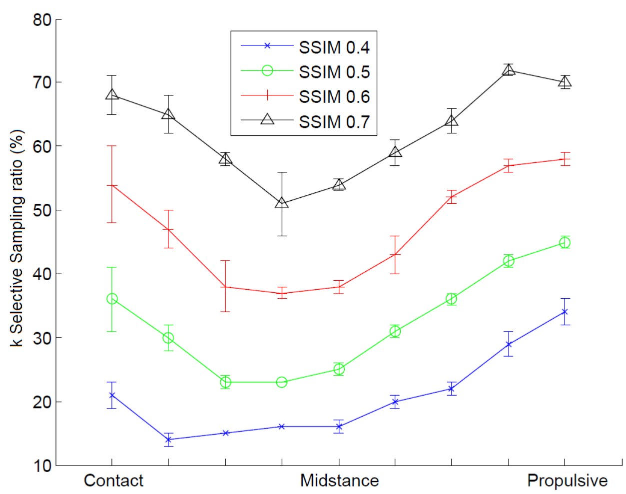

Figure 6.9: k selected samples vs phase cycle for various values of SSIM. Error bars indicate range of k values within 0.01 SSIM.

6.5.3.2 Energy Analysis

The important piece of evaluation is the energy efficiency improvement that this method provides. From Figs. 6.8 and 6.9, one can see that given the targeted SSIM, the sample number in different gait phases are different. This provides the opportunity to save more energy under some SSIM constraint. Table 6.1 shows the estimated battery life extension for variations in the reconstruction error. This is based on an initial estimate of 2 hours battery life of a 400mAh battery. The energy saving is calculated from the expected selective sampling ratio for each reconstructed frame at a certain SSIM. From Table 6.1, one can see that with 0.6 of the NMSE setup, the battery lifetime can be extracted to more than 12 hours, which is sufficient to support a one-day-time gait monitoring study. Also, the experimental result in the next section proves if the low-NMSE signal, one can still get good-quality gait features.

Table 6.1: Energy Savings Estimate

SSIM	Sampling Ratio	Battery Life*
1.0	100.0%	2.0 hr
0.9	69.0%	2.89 hr
0.8	45.3%	4.44 hr
0.7	26.2%	7.63 hr
0.6	19.1%	10.47 hr

*based on 400mAh battery

To further quantify the impact of k-selective sensing on different gait stages and its effect on power consumption, the pressure images from Contact, Midstance and Propulsive stages are investigated. Fig. 6.10 shows the NMSE values of these three images along with different k values. The information quality varies a lot with the change in selective sampling ratio in all three gait stages. Specifically, the image of Midstance always has low reconstruction error compared to the other two stages. It is because the foot pressure in Midstance is more widely distributed and forms a more structural shape. Also, one notices that the performance on Contact and Propulsive is close to each other in the entire k-selective sensing test. The result indicates that given a threshold of NMSE, a fairly large number of samples can be reduced according to different gait stages. For example, only 20% of sensor measurements are needed to reach 0.05 of NMSE in Midstance, but correspondingly 50% of sensor measurements are required in Contact and Propulsive. Accordingly, this gives evidence that the value of k can be adjusted through the gait cycle to allow a good trade off between reconstruction accuracy and power consumption of sensing.

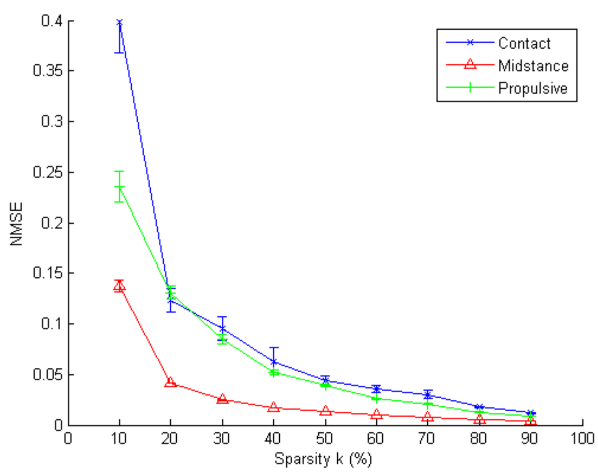

Figure 6.10: NMSE vs k selected samples for frames at Contact, Midstance and Propulsive stages. Error bars indicate variance across 500 frames.

6.5.3.3 Information Integrity on Gait Features

Finally, the impact of k-selective sensing on gait features is investigated. In this experiment, the pressure image data of one gait cycle with SSIM 1.0, 0.7 and 0.6 is used. For simplicity, one important gait feature, center of mass trajectory also known as gait-line [LF98], is chosen for the evaluation. Fig. 6.11 shows representative results of the center of mass trajectory calculated from the reconstructed images. Specifically, the red circle is the center of mass position in each pressure image, and the red curve is the trajectory formed by center of mass positions in the sequential pressure images. Although the calculated trajectories among different k-selective sensing setups are slightly different, it can preserve the important information in the feature, such as trajectory direction, transition and curvature. The result indicates that, in the case that algorithm SSIM is not high (such as 0.6), the features from reconstructed images are still good for gait analysis.

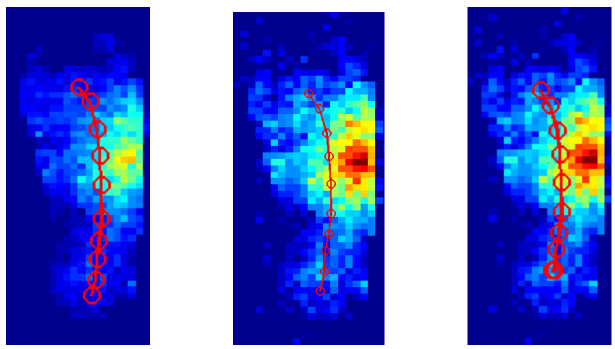

(a) (b) (c)

Figure 6.11: Trajectories of calculated center of mass of pressure image sequence using Local Randomized Selective Sensing with different SSIM values: (a) original SSIM 1.0, (b) reconstructed SSIM 0.7, (c) reconstructed SSIM 0.6.

Table 6.2 shows a summary of gait feature integrity. These results show that the extraction of gait features from reconstructed plantar pressure images do not degrade even with changes in the sampling ratio.

6.5.4 Conclusion and Future Work

An energy-efficient adaptive sensing framework is proposed. The method is based on gait stage analysis, and employ a k-selective sensing scheme to reduce the samples. The experimental results that this method can effectively reduce the number of samples required per frame and still offer good signal quality and gait

Table 6.2: Estimated Gait Feature Accuracy

Feature	Sampling Ratio	Accuracy
Gait-line, center of mass	20%	91.2%
	10%	88.6%
Gait-line velocity	20%	90.3%
	10%	89.3%
Cadence, steps per minute	20%	100%
	10%	100%
Heel strike location	20%	100%
	10%	93.6%

parameters after reconstruction.

CHAPTER 7

Final Summary

This dissertation presents a body of work in designing methods for analysis of pressure distribution images of the body. The main contributions in this work are summarized:

- A framework has been proposed for automatic sleep posture analysis using geometric feature extraction and sparse classification. A novel combination of geometric features and classification method has been applied to posture recognition using a pressure sensitive bedsheet.
- A framework to localize key bodyparts has been presented.
- A framework has been proposed to recognize pre-defined body motions on the bedsheet for the purpose of physical rehabilitation monitoring.
- An investigation of sensor sample reduction has been presented that allows images from the bedsheet to be reconstructed accurately from a minimal set of data points.

Applications such as pressure ulcer prevention, respiration monitoring, and rehabiliation exercise recognition were shown to be important. The methods contained have been verified in experiments, however further work in clinical trials will be needed for this technology to expand into hospitals and the home.

This work is a basis for future development in which the platform of a pressure sensitive bedsheet can be used for a wide variety of individualized medical applications. For posture analysis, a future direction could be the investigation of transitional states as subjects move between stable classified postures. Furthermore, 3D models of the human body can be applied to account for postures for instance when the subject is resting with knees up. For bodypart localization, tracking of key high risk areas is an important future goal in pressure ulcer monitoring. The sum of these advances will allow automatic notifications of impending risks to the patient as well as to the caregiver.

One final word is that an important part of these systems is feedback and education. It is generally known that feedback of progress is a good method of continued encouragement. These systems also provide education through multimedia and online coaching. The current trend is availability of information. All of the above systems have methods to communicate data into cloud networks typically through cell phone networks to the internet. Data can be stored in personalized electronic health record systems that can provide a complete longitudinal record of the patient's medical history. This information, with the correct authorization, can be accessed by medical professionals to provide the best ongoing healthcare.

The overall goal of ubiquitous personal health monitoring is an ambitious one and steps in the right direction are being taken to improve the quality of life for all.

References

[ALK] Cristina Ambrogio, Xazmin Lowman, Ming Kuo, Joshua Malo, Anil Prasad, and Sairam Parthasarathy. "Sleep and non-invasive ventilation in patients with chronic respiratory insufficiency." *Intensive Care Medicine*, **35**:306–313.

[APH10] Adriana M. Adami, Misha Pavel, Tamara L. Hayes, and Clifford M. Singer. "Detection of movement in bed using unobtrusive load cell sensors." *Transactions Infomation Technology in Biomedicine*, **14**(2):481, March 2010.

[Bak06] Richard Baker. "Gait Analysis Methods in Rehab." *Neoroengineering Rehabilitaion*, **3**(4):1–10, April 2006.

[Bat10] A. Bates. "Respiratory Rate and Flow Waveform Estimation from Tri-axial Accelerometer Data." In *Body Sensor Networks (BSN), 2010 International conference on*, pp. 144–150. IEEE press, 2010.

[BH07] Andrea L. Behrman and Susan J. Harkema. "Physical Rehabilitation as an Agent for Recovery After Spinal Cord Injury." *Physical Medicine and Rehab Clinics of North America*, **18**(2):183–202, 2007.

[Bil] Eli Billauer. "peakdet: Peak detection using MATLAB." `http://www.billauer.co.il/peakdet.html`.

[BKB09] Joonbum Bae, Kyoungchul Kong, Nancy Byl, and Masyoshi Tomizuka. "A Mobile Gait Monitoring System for Gait Analysis." In *IEEE Int. Conf. on Rehabilitation Robotics*, pp. 50–57, Kyoto, Japan, June 2009.

[Bor86] Gunilla Borgefors. "Distance transformations in digital images." *Computer vision, graphics, and image processing*, **34**(3):344–71, 1986.

[BRN10] F. Bianchi, S.J. Redmond, M.R. Narayanan, S. Cerutti, and N.H. Lovell. "Barometric Pressure and Triaxial Accelerometry-Based Falls Event Detection." *Neural Systems and Rehabilitation Engineering, IEEE Trans.*, **18**(6):619–627, 2010.

[Car08] J. Scott Cardozo. "New AASM Recommendations for Sensors: A Simple Guide for the Sleep Technologist." *Sleep Diagnosis and Therapy*, **21**(3), 2008.

[CAY06] M. Cocosila, N. Archer, and Y. Yuan. "Mobile Healthcare for Adherence: Business Considerations." *Mednet, Toronto, Canada, October*, pp. 13–20, 2006.

[CCB12] Shanshan Chen, Christopher Cunningham, Bradford Bennett, and John Lach. "Enabling Longitudinal Assessment of Ankle-Foot Orthosis Efficacy for Children with Cerebral Palsy." In *ACM Conference on Wireless Health*, pp. 1–10, San Diego, California, USA, October 2012.

[CDC] "Centers for Disease Control and Prevention.".

[CHY05] Yongjoon Chee, Jooman Han, Jaewoong Youn, and Kwangsuk Park. "Air mattress sensor system with balancing tube for unconstrained measurement of respiration and heart beat movements." *Physiological Measurement*, **26**(4):413, 2005.

[Com04] ITAA E-Health Committee. "Chronic Care Improvement: How Medicare Transformation Can Save Lives, Save Money, and Stimulate an Emerging Technology Industry." *ITAA E-Health White paper*, 2004.

[Cov] Covidien. "Nellcor Bedside Respiratory Patient Monitoring System." `http://www.covidien.com`.

[CRT06] E.J. Candes, J. Romberg, and T. Tao. "Robust uncertainty principles: exact signal reconstruction from highly incomplete frequency information." *Information Theory, IEEE Transactions*, **52**(2):489–509, Feb. 2006.

[CT91] Thomas M. Cover and Joy A. Thomas. *Elements of information theory.* Wiley-Interscience, New York, NY, USA, 1991.

[CVX12] CVX Research Inc. "CVX: Matlab Software for Disciplined Convex Programming, version 2.0." `http://cvxr.com/cvx`, August 2012.

[CZN05] Wenxi Chen, X Zhu, Tetsu Nemoto, Yumi Kanemitsu, Keiichiro Kitamura, and Ken-ichi Yamakoshi. "Unconstrained detection of respiration rhythm and pulse rate with one under-pillow sensor during sleep." *Medical and Biological Engineering and Computing*, **43**(2):306–312, 2005.

[DDK09] Stuti Dang, Susan Dimmick, and Geetanjali Kelkar. "Evaluating the Evidence Base for the Use of Home Telehealth Remote Monitoring in Elderly with Heart Failure." *Telemedicine and e-Health*, **15**:v, October 2009.

[DeM07] Susan DeMeulenaere. "Pulse Oximetry: Uses and Limitations." *The Journal for Nurse Practitioners*, **3**(5):312–7, 2007.

[DF01] Quentin Delamarre and Olivier Faugeras. "3D Articulated Models and Multiview Tracking with Physical Forces." *Computer Vision and Image Understanding*, **81**(3):328–357, 2001.

[DHH01] “Steps to a healthier U.S. Washington (DC): Office of Public Health Promotion.” *U.S. Department of Health and Human Services*, 2001.

[Don06] D.L. Donoho. “Compressed sensing.” *Information Theory, IEEE Trans.*, **52**(4):1289–1306, 2006.

[Eys01] G. Eysenbach. “What is e-health?” *J Med Internet Res*, **3**(2):e20, Jun 2001.

[FB02] Ronan Fablet and Michael J. Black. “Automatic Detection and Tracking of Human Motion with a View-Based Representation.” In *Proceedings of the 7th European Conference on Computer Vision-Part I*, pp. 476–491, 2002.

[FCE01] M Fransen, J Crosbie, and J Edmonds. “Physical therapy is effective for patients with osteoarthritis of the knee: a randomized controlled clinical trial.” *Journal of Rheumatology*, **28**(1):156, 2001.

[FE73] Martin A Fischler and Robert A Elschlager. “The representation and matching of pictorial structures.” *IEEE Transactions on Computers*, **22**(1):67–92, 1973.

[FH05] Pedro F Felzenszwalb and Daniel P Huttenlocher. “Pictorial structures for object recognition.” *International Journal of Computer Vision*, **61**(1):55–79, 2005.

[FMG12] N. Foubert, A.M. McKee, R.A. Goubran, and F. Knoefel. “Lying and sitting posture recognition and transition detection using a pressure sensor array.” In *Medical Measurements and Applications Proceedings (MeMeA), 2012 IEEE International Symposium*, pp. 1–6, 2012.

[FYB13] M. Farshbaf, Rasoul Yousefi, M. Baran Pouyan, Sarah Ostadabbas, Mehrdad Nourani, and Matthew Pompeo. “Detecting High-Risk Regions for Pressure Ulcer Risk Assessment.” In *International Conference on Bioinformatics and Biomedicine*. IEEE, 2013.

[GS08] D. Gouwanda and S.M.N.A. Senanayake. “Emerging Trends of Body-Mounted Sensors in Sports and Human Gait Analysis.” In NoorAzuan Abu Osman, Fatimah Ibrahim, WanAbuBakar Wan Abas, Herman-Shah Abdul Rahman, and Hua-Nong Ting, editors, *4th Kuala Lumpur Int. Conf. on Biomedical Engineering 2008*, volume 21 of *IFMBE Proceedings*, pp. 715–718. Springer Berlin Heidelberg, 2008.

[GSH11] Robert Grimm, Johann Sukkau, Joachim Hornegger, and Gunther Greiner. “Automatic Patient Pose Estimation Using Pressure Sensing Mattresses.” In *Bildverarbeitung fur die Medizin 2011*, Informatik aktuell. 2011.

[HDS10] Enamul Hoque, Robert F. Dickerson, and John A. Stankovic. "Monitoring body positions and movements during sleep using WISPs." In *Wireless Health 2010*, WH '10, pp. 44–53, 2010.

[HHC08] Chi-Chun Hsia, Yu-Wei Hung, Yu-Hsien Chiu, and Chia-Hao Kang. "Bayesian classification for bed posture detection based on kurtosis and skewness estimation." In *e-health Networking, Applications and Services, 2008. HealthCom 2008. 10th International Conference on*, pp. 165–168, July 2008.

[Hil] Hillrom. `http://www.hill-rom.com`.

[HKV02] Timothy J Hodgetts, Gary Kenward, Ioannis G Vlachonikolis, Susan Payne, and Nicolas Castle. "The identification of risk factors for cardiac arrest and formulation of activation criteria to alert a medical emergency team." *Resuscitation*, **54**(2):125–131, 2002.

[HLA09] C.C. Hsia, K.J. Liou, A.P.W. Aung, V. Foo, W. Huang, and J. Biswas. "Analysis and comparison of sleeping posture classification methods using pressure sensitive bed system." In *Engineering in Medicine and Biology Society, 2009. EMBC 2009. Annual International Conference of the IEEE*, pp. 6131–6134, Sept. 2009.

[HS10] David Heise and Marjorie Skubic. "Monitoring pulse and respiration with a non-invasive hydraulic bed sensor." In *Engineering in Medicine and Biology Society (EMBC), 2010 Annual International Conference of the IEEE*, pp. 2119–2123. IEEE, 2010.

[HSM00] T. Harada, T. Sato, and T. Mori. "Human motion tracking system based on skeleton and surface integration model using pressure sensors distribution bed." In *Proc. Workshop on Human Motion*, p. 99, 2000.

[HTW10] A. Hart, K. Tallevi, D. Wickland, R.E. Kearney, and J.A. Cafazzo. "A contact-free respiration monitor for smart bed and ambulatory monitoring applications." In *Engineering in Medicine and Biology Society (EMBC), 2010 Annual International Conference of the IEEE*, pp. 927–930, 2010.

[HXS12] Ming-Chun Huang, Wenyao Xu, Yi Su, Belinda Lange, Chien-Yen Chang, and Majid Sarrafzadeh. "SmartGlove for upper extremities rehabilitative gaming assessment." In *Proceedings of the 5th International Conference on Pervasive Technologies Related to Assistive Environments*, pp. 20:1–20:4, 2012.

[Idz03] C. Idzikowski. *Beating Insomnia: How to Get a Good Night's Sleep*. Gill & MacMillan, 2003.

[JGK06] M.H. Jones, R. Goubran, and F. Knoefel. "Identifying Movement Onset Times for a Bed-Based Pressure Sensor Array." In *Medical Measurement and Applications. MeMea IEEE International Workshop*, pp. 111–114, April 2006.

[JKP94] George H. John, Ron Kohavi, and Karl Pfleger. "Irrelevant Features and the Subset Selection Problem." In *Machine Learning: Procs. 11th International Conference*, pp. 121–129. Morgan Kaufmann, 1994.

[JMO05] E. Jovanov, A. Milenkovic, C. Otto, P. de Groen, B. Johnson, S. Warren, and G. Taibi. "A WBAN System for Ambulatory Monitoring of Physical Activity and Health Status: Applications and Challenges." In *27th Annual International Conference of the Engineering in Medicine and Biology Society*, pp. 3810–3813, Jan. 2005.

[Jol] I.T. Jolliffe. *Principal Component Analysis.* Springer Series in Statistics.

[KAO06] Y. Kishimoto, A. Akahori, and K. Oguri. "Estimation of sleeping posture for M-Health by a wearable tri-axis accelerometer." In *Medical Devices and Biosensors. 3rd IEEE/EMBS International Summer School*, pp. 45–48, Sept. 2006.

[KGG94] Vipin Kumar, Ananth Grama, Anshul Gupta, and George Karypis. *Introduction to parallel computing: design and analysis of algorithms.* Benjamin-Cummings Publishing Co., Inc., Redwood City, CA, USA, 1994.

[KKW64] E. Kinnen, W. Kubicek, D. Witsoe, R. Patterson, and USAF School of Aerospace Medicine. *Thoracic Cage Impedance Measurements: Impedance Plethysmographic Determination of Cardiac Output (an Interactive Study).* Technical documentary report, SAM-TDR. USAF School of Aerospace Medicine - Aerospace Medical Division (AFSC), 1964.

[KNP01] E. Krupinski, M. Nypaver, and R. Poropatich. "Telemedicine/telehealth: An international perspective. Clinical applications in telemedicine/telehealth." *Telemed J E Health*, **8**(1):13–34, 2001.

[KVA00] H. I. Krebs, B. T. Volpe, M. L. Aisen, and N. Hogan. "Increasing productivity and quality of care : Robot-aided neuro-rehabilitation." *Rehabilitation Research & Development*, **37**:639, Nov 2000.

[KW78] J.B. Kruskal and M. Wish. *Multidimensional Scaling.* Sage University Paper series on Quantitative Applications in the Social Sciences, 07-011, Beverly Hills and London: Sage Publications, 1978.

[LB13] B. Lee and G. Butler. "Methods and systems for monitoring a patient to reduce the incidence of pressure ulcers.", October 24 2013. WO Patent App. PCT/US2013/037,494.

[LF98] C. Lee and C. Farley. "Determinants of the center of mass trajectory in human walking and running." *The Journal of Experimental Biology*, **13**(1):2935–2944, January 1998.

[LGL] Yiguang Liu, Shuzhi Sam Ge, Chunguang Li, and Zhisheng You. "k-NS: A Classifier by the Distance to the Nearest Subspace." *Trans. Neural Networks*.

[LHL13] H. Lee, S. Hwang, S. Lee, Y. Lim, and K. Park. "Estimation of Body Postures on Bed Using Unconstrained ECG Measurements." *Biomedical and Health Informatics, IEEE Journal*, **PP**(99):1–1, 2013.

[LIS09] Tao Liu, Yoshio Inoue, and Kyto Shibata. "Development of a Wearable Sensor System for Quantitative Gait Analysis." *Measurement*, **42**(7):978–988, Feb 2009.

[LJN12] Michelle Lusardi, Milagros Jorge, and Caroline Nielsen. *Orthotics and Prosthetics in Rehab.* Elsevier, St. Louis, Missouri, 2012.

[LMK13] RK Lord, CR Mayhew, R Korupolu, EC Mantheiy, MA Friedman, JB Palmer, and DM Needham. "ICU Early Physical Rehabilitation Programs: Financial Modeling of Cost Savings." *Critical Care Medicine*, Jan. 2013.

[Low04] David G. Lowe. "Distinctive Image Features from Scale-Invariant Keypoints." *Int. J. Comput. Vision*, **60**(2):91–110, November 2004.

[LPH09] J. B. Lee, Y. H. Park, J. H. Hong, S. H. Lee, K. H. Jung, J. H. Kim, H. Yi, and C. Shin. "Determining optimal sleep position in patients with positional sleep-disordered breathing using response surface analysis." *Journal of Sleep Research*, **18**(1):26–35, 2009.

[LSH09] Qiang Li, J.A. Stankovic, M.A. Hanson, A.T. Barth, J. Lach, and Gang Zhou. "Accurate, Fast Fall Detection Using Gyroscopes and Accelerometer-Derived Posture Information." In *Wearable and Implantable Body Sensor Networks. 6th Int. Workshop*, pp. 138–143, 2009.

[LXH12] Zhinan Li, Wenyao Xu, Anpeng Huang, and M. Sarrafzadeh. "Dimensionality Reduction for Anomaly Detection in Electrocardiography: A Manifold Approach." In *Wearable and Implantable Body Sensor Networks (BSN), 2012 Ninth International Conference*, pp. 161–165, 2012.

[LXH13] Jason J. Liu, Wenyao Xu, Ming-Chun Huang, Nabil Alshurafa, and Majid Sarrafzadeh. "A Dense Pressure Sensitive Bedsheet Design for Unobtrusive Sleep Posture Monitoring." In *IEEE International Conference on Pervasive Computing and Communications*, Mar 2013.

[LY08] Wen-Hung Liao and Chien-Ming Yang. "Video-based activity and movement pattern analysis in overnight sleep studies." In *Pattern Recognition, 2008. ICPR 2008. 19th International Conference*, pp. 1–4, Dec. 2008.

[MMR11] I. Main, R. Miller, T. Russel, and M. Ousdahl. "Risk modeling for pressure ulcer formation.", August 4 2011. WO Patent App. PCT/CA2011/000,098.

[MPT04] R. Murthy, I. Pavlidis, and P. Tsiamyrtzis. "Touchless monitoring of breathing function." In *Annual International Conference of the IEEE Engineering in Medicine and Biology Society*, 2004.

[NAH10] Hyduke Noshadi, Shaun Ahmadian, Hagop Hagopian, Jonathan Woodbridge, Foad Dabiri, Navid Amini, Majid Sarrafzadeh, and Nick Terrafranca. "Hermes - Mobile Balance and Instability Assessment System." *Proc. BIOSIGNALS*, pp. 264–270, 2010.

[Nat95] B. K. Natarajan. "Sparse Approximate Solutions to Linear Systems." *SIAM J. Comput.*, **24**(2):227–234, April 1995.

[NAZ10] Hongbo Ni, Bessam Abdulrazak, Daqing Zhang, and Shu Wu. "Unobtrusive sleep posture detection for elder-care in smart home." In *Proceedings of the Aging friendly technology for health and independence, and 8th international conference on Smart homes and health telematics*, ICOST'10, pp. 67–75, 2010.

[NMT] K. Nakajima, Y. Matsumoto, and T. Tamura. "A monitor for posture changes and respiration in bed using real time image sequence analysis." In *Engineering in Medicine and Biology Society, 2000. Proc. 22nd IEEE*, volume 1, pp. 51–54.

[NMT01] Kazuki Nakajima, Yoshiaki Matsumoto, and Toshiyo Tamura. "Development of real-time image sequence analysis for evaluating posture change and respiratory rate of subject in bed." *Physiological Meas.*, **22**(3), 2001.

[NMW11] M. Nishyama, M. Miyamoto, and K. Watanabe. "Respiration and body movement analysis during sleep in bed using hetero-core fiber optic pressure sensors without constraint to human activity." *Journal of Biomedical Optics*, **16**(1):17002–7, 2011.

[NW06] S.M. Nettina and Lippincott Williams & Wilkins. *The Lippincott Manual of Nursing Practice*. Lippincott Williams & Wilkins, 2006.

[OEC12] "Organisation for Economic Co-operation and Development.", 2012.

[OGF08] Carsten Orwat, Andreas Graefe, and Timm Faulwasser. "Towards pervasive computing in health care - A literature review." *BMC Medical Informatics and Decision Making*, **8**(1):26, 2008.

[OS06] Arie Oksenberg and Donald Silverberg. "The Effect of Body Posture on Sleep-Related Breathing Disorders: Facts and Therapeutic Implications." *Sleep Medicine Reviews*, **2**(3):139–162, 2006.

[OYF11] Sarah Ostadabbas, Rasoul Yousefi, Miad Faezipour, Mehrdad Nourani, and Matthew Pompeo. "Pressure ulcer prevention: An efficient turning schedule for bed-bound patients." In *Life Science Systems and Applications Workshop (LiSSA), 2011 IEEE/NIH*, pp. 159–162. IEEE, 2011.

[Par09] James Parish. "Sleep-Related Problems in Common Medical Conditions." *Chest Journal*, **135**(2):563–572, 2009.

[Phi] Philips. "Vital Signs Camera." `http://www.vitalsignscamera.com`.

[PHR98] Thomas Perneger, Celiane Heliot, Anne-Claire Rae, Francois Borst, and Jean-Michel Gaspoz. "Hospital-acquired pressure ulcers: Risk factors and use of preventive devices." *Archives of Internal Medicine*, **158**(17):1940–1945, 1998.

[PKO03] MA. Peberdy, W. Kaye, JP. Ornato, GL. Larkin, V. Nadkarni, ME. Mancini, RA. Berg, G. Nichol, and T. Lane-Trultt. "Cardiopulmonary resuscitation of adults in the hospital: a report of 14720 cardiac arrests from the National Registry of Cardiopulmonary Resuscitation." *Resuscitation*, **58**(3):297–308, 2003.

[PMP10] Ming-Zher Poh, Daniel J. McDuff, and Rosalind W. Picard. "Non-contact, automated cardiac pulse measurements using video imaging and blind source separation." *Optics Express*, **18**, 2010.

[PRK93] Y.C. Pati, R. Rezaiifar, and P. S. Krishnaprasad. "Orthogonal matching pursuit: recursive function approximation with applications to wavelet decomposition." In *Signals, Systems and Computers. Conf. Record of The 27th Asilomar Conf.*, pp. 40–44 vol.1, 1993.

[QB08] Muhannad Quwaider and Subir Biswas. "Body posture identification using hidden Markov model with a wearable sensor network." In *Proceedings of the ICST 3rd international conference on Body area networks*, BodyNets '08, pp. 19:1–19:8, 2008.

[Rab89] Lawrence R. Rabiner. "A tutorial on hidden markov models and selected applications in speech recognition." In *Proceedings of the IEEE*, pp. 257–286, 1989.

[RM11] Kristin Reed and Rick May. "HealthGrades Seventh Annual Patient Safety in American Hospitals Study." *HealthGrades, Inc.*, 2011.

[SA02] A. Sadeh and C. Acebo. "The Role of Actigraphy in Sleep Medicine." *Sleep Medicine Reviews*, **135**(2):217–226, 2002.

[SCF06] J Stevens, P Corso, E Finkelstein, and T Miller. "The costs of fatal and nonfatal falls among older adults." *Injury Prevention*, **12**:290295, 2006.

[Sec] SecuraTrac. "SecuraFone Health." `http://www.securafone.com/subpages/health.php`.

[SR03] Lawrence Saul and Sam Roweis. "Think globally, fit locally: unsupervised learning of low dimensional manifolds." *Journal of Machine Learning Research*, **4**:119–155, Dec. 2003.

[SV09] Sweta Sneha and Upkar Varshney. "Enabling ubiquitous patient monitoring: Model, decision protocols, opportunities and challenges." *Decision Support Systems*, **46**(3):606 – 619, 2009.

[Tek] Tekscan. `http://www.tekscan.com`.

[TG07] J.A. Tropp and A.C. Gilbert. "Signal Recovery From Random Measurements Via Orthogonal Matching Pursuit." *Information Theory, IEEE Trans.*, **53**(12):4655–4666, 2007.

[TH03] Yaqing Tao and Huosheng Hu. "Buiding a Visual Tracking System for Home-Based Rehabilitation." In *In Proceedings of the 9th Chinese Automation and Computing Society Conference In the UK*, pp. 343–348, 2003.

[Tha06] Michael Thase. "Depression and Sleep: Pathophysiology and Treatment." *Dialogues in Clinical Neurosciences*, **135**(2):217–226, 2006.

[TSL00] Joshua B. Tenenbaum, Vin de Silva, and John C. Langford. "A Global Geometric Framework for Nonlinear Dimensionality Reduction." **290**(5500):2319–2323, 2000.

[VHW11] Vincent Verhaert, Bart Haex, Tom De Wilde, Daniel Berckmans, Marie Vandekerckhove, Johan Verbraecken, and Jos Vander Sloten. "Unobtrusive Assessment of Motor Patterns During Sleep Based on Mattress Indentation Measurements." *IEEE Transactions on Information Technology in Biomedicine*, **15**(5):787–794, 2011.

[Vis] VistaMedical. `http://www.pressuremapping.com`.

[WBS04] Zhou Wang, A.C. Bovik, H.R. Sheikh, and E.P. Simoncelli. "Image quality assessment: from error visibility to structural similarity." *Image Processing, IEEE Trans.*, **13**(4):600–612, 2004.

[Wei94] W. Wei. *Time Series Analysis*. Addison-Wesley Publishing Company, New York, 1994.

[Wei99] Mark Weiser. "The computer for the 21st century." *SIGMOBILE Mob. Comput. Commun. Rev.*, **3**(3):3–11, July 1999.

[XBW12] Xiaoyu Xu, M. Batalin, Yan Wang, and W. Kaiser. "Gait quality evaluation method for post-stroke patients." In *Acoustics, Speech and Signal Processing (ICASSP), IEEE Int. Conf.*, pp. 613–616, 2012.

[XGL12] W. Xu, C. Gu, C. Li, and M. Sarrafzadeh. "Robust Doppler radar demodulation via compressed sensing." *Electronics Letters*, **48**(22):1428–1430, 2012.

[XHA12] W. Xu, M.C. Huang, N. Amini, J.J. Liu, L. He, and M. Sarrafzadeh. "Smart Insole: A Wearable System for Gait Analysis." *PETRAE*, 2012.

[XLH11] Wenyao Xu, Zhinan Li, Ming-Chun Huang, N. Amini, and M. Sarrafzadeh. "eCushion: An eTextile Device for Sitting Posture Monitoring." In *IEEE Conference on Body Sensor Networks (BSN)*, pp. 194–199, May 2011.

[Xse] Xsensor. `http://www.xsensor.com`.

[XZS12] Wenyao Xu, Mi Zhang, A.A. Sawchuk, and M. Sarrafzadeh. "Co-recognition of Human Activity and Sensor Location via Compressed Sensing in Wearable Body Sensor Networks." In *Wearable and Implantable Body Sensor Networks (BSN)*, pp. 124–129, May 2012.

[YHW09] Marcus Yip, DD He, Eric Winokur, Amanda Gaudreau Balderrama, Robert Sheridan, and Hongshen Ma. "A flexible pressure monitoring system for pressure ulcer prevention." In *International Conference of IEEE Engineering in Medicine and Biology Society, EMBC*, pp. 1212–5. IEEE, 2009.

[YOF11] R. Yousefi, S. Ostadabbas, M. Faezipour, M. Farshbaf, M. Nourani, L. Tamil, and M. Pompeo. "Bed posture classification for pressure ulcer prevention." In *Engineering in Medicine and Biology Society*, pp. 7175–7178, Sept. 2011.

[ZH08] Huiyu Zhou and Huosheng Hu. "Human motion tracking for rehabilitation - A survey." *Biomedical Signal Proc. and Control*, **3**:1–18, 2008.

[ZS11] Mi Zhang and A.A. Sawchuk. "Manifold Learning and Recognition of Human Activity Using Body-Area Sensors." In *Machine Learning and Apps and Workshops (ICMLA), 10th Int. Conf.*, volume 2, pp. 7–13, Dec. 2011.